JOURNAL OF PETROLOGY

Journal of Petrology, 2016, Vol. 57, No. 9, 1833–1864
doi: 10.1093/petrology/egw063
Original Article

OXFORD

From Passive Degassing to Violent Strombolian Eruption: the Case of the 2008 Eruption of Llaima Volcano, Chile

Dawn C. S. Ruth[1,2]*, Elizabeth Cottrell[2], Joaquín A. Cortés[3,4], Katherine A. Kelley[5] and Eliza S. Calder[3]

[1]Department of Geology, State University of New York at Buffalo, Buffalo, NY 14260, USA; [2]Smithsonian Institution, National Museum of Natural History, Washington, DC, 20560, USA; [3]School of GeoSciences, University of Edinburgh, Edinburgh EH9 3FE, UK; [4]School of Civil Engineering and Geosciences, Newcastle University, Newcastle NE1 7RU, UK and [5]Graduate School of Oceanography, University of Rhode Island, Narragansett, RI 02882, USA

*Corresponding author. Present address: Earth Observatory of Singapore, Nanyang Technological University, Singapore, 639798. E-mail: sdawn@ntu.edu.sg

Received June 28, 2015; Accepted September 19, 2016

ABSTRACT

On 1 January 2008 Llaima volcano, a basaltic andesite stratocone in southern Chile, entered a phase of violent Strombolian eruption. Llaima, like many passively degassing systems, has experienced prolonged (decades-long) periods of persistent summit degassing from its open vent. The rapid transition from long-lived passive degassing to violent explosive eruption occurred with limited precursory monitoring signals. This study is motivated by the desire to understand what occurs in these systems when that switch takes place. To this end, we study the products of the 2008 violent Strombolian eruption of Llaima volcano. We present new textural analyses of scoria and geochemical data for five whole-rock samples, troctolite glomerocrysts with and without Cr-spinel, and 182 olivine-hosted melt inclusions from tephra samples. Two populations of scoria ('brown' and 'black') are distinguished by their variable crystallinity and vesicularity, but are geochemically indistinguishable. Black scoria contains abundant microlites with tabular to acicular morphologies and convolute vesicles up to 1·75 mm in effective diameter. The brown scoria tends to have fewer, acicular microlites, abundant matrix glass, and round vesicles with a narrower size distribution, constrained to $<0{\cdot}4$ mm in diameter. Overall, the textures of the black and brown scoria provide evidence for a textural maturation process in which shallow system magma becomes more crystal rich and probably rheologically stiffer as a result of prolonged passive degassing. The Cr-spinel-bearing and Cr-spinel-free troctolite glomerocrysts have plagioclase and olivine compositions of $An_{65–92}$ and Fo_{81}, respectively. The Cr# in the Cr-spinel ranges from 26 to 37, consistent with magma originating from the deeper plumbing system. Whole-rock compositions for the tephra average 51 wt % SiO_2, 18 wt % Al_2O_3, and ~6 wt % MgO. The major element compositions of olivine-hosted melt inclusions range from 49 to 56 wt % SiO_2 and 3·72 to 7·76 wt % MgO; there is no distinct compositional difference between olivine-hosted melt inclusions sourced from the different scoria. Melt inclusion volatile contents range from below detection to 2·95 wt % H_2O and 1973 ppm CO_2 (though not in the same melt inclusion). H_2O and CO_2 concentrations are consistent with open-system degassing and, when compared with differentiation indices (e.g. K_2O), indicate coupled degassing and crystallization throughout the system. The majority of melt inclusions define a single liquid line of descent indicative of plagioclase and olivine fractionation. Entrapment pressures range from 8 to 342 MPa and fall into two groups: 8–100 MPa (300 m to ~4 km depth) and >100 MPa (4–14 km depth), revealing that this eruption tapped a deep plumbing system. We propose here that passive degassing at Llaima is maintained by periodic, small-batch magma injections. Consequently, owing to extensive degassing the upper plumbing system magma crystallized and increased in viscosity. Before the 2008 eruption,

some volatiles sourced from the repeatedly injected magmas exsolved from the inferred crystal mush and ascending from deeply sourced degassing magmas, and gradually accumulated within the crystal mush and beneath the stiffened conduit magma. Our results support a model in which eruption triggering occurred when magma injection remobilized the mush and, importantly, unlocked the accumulated gases, which ascended rapidly and generated the observed violent Strombolian explosive activity. Our proposed model contrasts with those models for explosive mafic volcanism that require rapid magma ascent under closed-system degassing conditions. Importantly, our proposed mechanism provides a means for systems with dominantly open-system degassing behavior to switch from passive degassing to explosive eruptions.

Key words: basaltic andesite; eruption trigger; magma recharge; melt inclusions; open vent volcanism; passive degassing; regulated gas transport

INTRODUCTION

On 1 January 2008, Llaima volcano in the Southern Andean Volcanic Zone, Chile, entered a new phase of intense explosive activity. The eruption, described as a violent Strombolian-type eruption, was characterized by highly pulsatory fire fountaining and the development of a 10 km high ash plume (Ruth & Calder, 2014). Prior to the eruption the volcano had exhibited persistent passive degassing, at least since its previous eruption in 1994 (ONEMI, 2009). Passive degassing (sometimes called persistent degassing, or quiescent degassing) is characterized by volatile outgassing, usually from a summit vent, but is commonly associated with limited or negligible net magma flux out of the system. In many cases volcanoes exhibiting this behavior are typified by mafic magmas and open vents, and the persistent degassing can continue for months to years (Rosi *et al.*, 2000; Rose *et al.*, 2013). In contrast, violent Strombolian eruptions (often referred to as paroxysms, or cineritic eruptions) are characterized by moderate-sized, sustained ash plumes (>10 km in altitude) and dispersed tephra deposits (Francis *et al.*, 1990; Houghton & Gonnermann, 2008; Valentine & Gregg, 2008). Violent Strombolian eruptions are known to occur periodically at volcanoes that commonly present passive degassing, including Stromboli, Italy (Barberi *et al.*, 1993; Rosi *et al.*, 2000, 2013); Llaima and Villarrica, in Chile (Petit-Breuilh, 2006; ONEMI, 2009), Masaya, Nicaragua (Williams, 1983); and Fuego, Guatemala (Rose *et al.*, 2008). Where these violent explosive eruptions occur from open, already passively degassing systems, their onset can be sudden, sometimes with little to no advance warning or signals in monitoring data. The hazards associated with such events (ballistics, tephra fall, lava flows, and sometimes lahars) can be challenging to ameliorate because of the sudden onset nature, especially if the volcano is located in a region of high population (e.g. Rose *et al.*, 2008, 2013; Rosi *et al.*, 2013). Understanding the mechanisms that initiate this rapid change in behavior, from passive degassing to violent explosive activity, is therefore a key challenge to improving our capacity to deal with explosive basaltic volcanism.

Investigations on this style of explosive basaltic volcanism have been undertaken at Stromboli, Mt Etna, Parícutin, and Cerro Negro (Allard, 1997; Roggensack *et al.*, 1997; Métrich *et al.*, 2001, 2010; Lautze & Houghton, 2007; Pioli *et al.*, 2008; Johnson *et al.*, 2010). Violent Strombolian eruptions necessitate not only high mass fluxes of magma (e.g. mass eruption rates 10^3–10^5 kg s^{-1}), but also, critically, high instantaneous gas fluxes (Pioli *et al.*, 2008, 2009). In several eruption cases, the triggering of these events has been attributed to bouts of recharge of mafic magma that ascends rapidly through the system; for example, Stromboli (Métrich *et al.*, 2001, 2010; Bertagnini *et al.*, 2003), Parícutin (Luhr, 2001; Pioli *et al.*, 2008), and Cerro Negro (Roggensack *et al.*, 1997). Deeply sourced magma injection into a relatively shallow reservoir is inferred from the volatile contents of mineral-hosted melt inclusions. The inferred rapid, closed-system ascent and subsequent degassing of H_2O in these magmas then drives the sporadic explosive eruptions, often producing texturally bimodal scoria populations with chemically distinct olivine-hosted melt inclusions (e.g. Métrich *et al.*, 2010). However, this model does not work for systems in which the erupted products record dominantly open-system degassing behavior (e.g. Anak Krakatau, Mandeville *et al.*, 1998), or systems that are not well characterized by either closed- or open-system degassing (e.g. Johnson *et al.*, 2010; Oppenheimer *et al.*, 2011). Alternative mechanisms that have been proposed to explain the transition from passive degassing or low-intensity eruptions to violent explosive eruptions include changes in magma system geometry (Genereau *et al.*, 2010; Palma *et al.*, 2011) and changes in the fluid dynamics during magma ascent (Jaupart, 1998; Houghton & Gonnermann, 2008).

Studies of the products of the 2008 eruption of Llaima have been undertaken by Bouvet de Maisonneuve *et al.* (2012*a*, 2012*b*) and Ruth & Calder (2014). Ruth & Calder (2014) reported on the morphological, textural and dispersal characteristics of the diverse tephra types, including distinctive plate tephra. Bouvet de Maisonneuve *et al.* (2012*a*) reported olivine-hosted melt inclusion data for the 2008 scoria, as well as for three historical eruptions in AD 1957 and ~1850

(separated into upper and lower tephras). Their melt inclusion dataset provides evidence for a persistent shallow plumbing system ($< \sim$130 MPa) throughout this time, but provides limited evidence for consistent degassing and fractionation trends. For the 2008 eruption, mineral zoning and chemistry data suggest repeated pre-eruption magma injection (Bouvet de Maisonneuve *et al.*, 2012*b*). Based on these findings, Bouvet de Maisonneuve *et al.* proposed that the 2008 eruption was triggered by remobilization of a crystal mush (i.e. magmatic regions with >50% crystals) by magma recharge. The Bouvet de Maisonneuve *et al.* (2012*a*, 2012*b*) study provides an excellent framework for understanding reservoir processes associated with several of the recent major eruptive episodes at Llaima, but key aspects of the 2008 eruption remain unaccounted for.

In this work we focus specifically on the products of the 2008 eruption. We extend the work undertaken by both Bouvet de Maisonneuve *et al.* (2012*a*, 2012*b*) and Ruth & Calder (2014) and use combined textural and geochemical analysis that both complements previous work and provides new information about the shallow and deeper system. Specifically, we build on the previous work in the following ways.

1. Ruth & Calder (2014) identified texturally heterogeneous tephra produced during the violent explosive phase of the 2008 eruption. Here we use textural data, including vesicle and crystal size distributions, from these different tephra to investigate crystallization and degassing processes in the shallow system and discuss these in the context of the explosive eruptive activity. This information is important because shallow degassing and crystallization are considered critical processes that can lead to increases in the intensity of mafic eruptions (e.g. Sable *et al.*, 2006; Houghton & Gonnermann, 2008).
2. For the different tephra types we provide major, trace, and volatile element data for 182 olivine-hosted melt inclusions, thereby extending the work of Bouvet de Maisonneuve *et al.* (2012*a*, 2012*b*). Our comprehensive geochemical data show evidence of a deeper, more CO_2-rich plumbing system than previously reported.
3. We consider it important that any conceptual model for the Llaima plumbing system places the 2008 eruptive episode in the context of the persistently active passive degassing system, which typified the activity both before that eruption occurred and afterwards. Although Bouvet de Maisonneuve *et al.* (2012*a*, 2012*b*) focused dominantly on the nature of the magmatic plumbing and crystal mush processes, the role of gas accumulation was not investigated. Here, bearing in mind that high gas fluxes resulting in highly pulsatory lava fountaining are a key driver of violent Strombolian eruptions (e.g. Pioli *et al.*, 2009), we discuss potential scenarios for gas accumulation within the Llaima plumbing system. Finally we propose a model for the transition in activity style from passive degassing to violent explosive eruptions.

LLAIMA VOLCANO AND THE 1 JANUARY 2008 ERUPTION

Llaima volcano [38°41′45S, 71°43′54W, 3179 m above sea level (a.s.l.)] is a basaltic andesite stratocone located in the Southern Volcanic Zone (SVZ) of the Chilean Andes about ~600 km south of Santiago (Fig. 1). Llaima is one of the most historically active volcanoes in the SVZ with 54 eruptions since 1640 (Naranjo & Moreno, 2005; Petit-Breuilh, 2006). Statistical analysis of the historical record for eruptions of volcanic explosivity index (VEI) $\geq$ 2 indicates an eruption recurrence interval of ~6 years (Dzierma & Wehrmann, 2010). Major explosive activity producing significant eruption plumes (>10 km) and associated tephra deposits occurred most recently in 1957 (Hantke, 1962; Naranjo & Moreno, 2005), with a similar, but lower intensity eruption occurring in May 1994 (Moreno & Fuentealba, 1994). The 1994 eruption lasted 8 h, produced lava fountains, a 7 km altitude plume and associated tephra deposit, and lahars down the western flanks; the eruption was characterized at VEI 2 (Moreno & Fuentealba, 1994).

On 1 January 2008, between 1730 and 1820 local time (GMT –04:00), a summit eruption began at Llaima. The eruption was characterized by violent pulsating Strombolian and fire fountaining activity, which produced a plume reaching ~11 km high. Lava flows were generated on the west flank, and lahars were generated

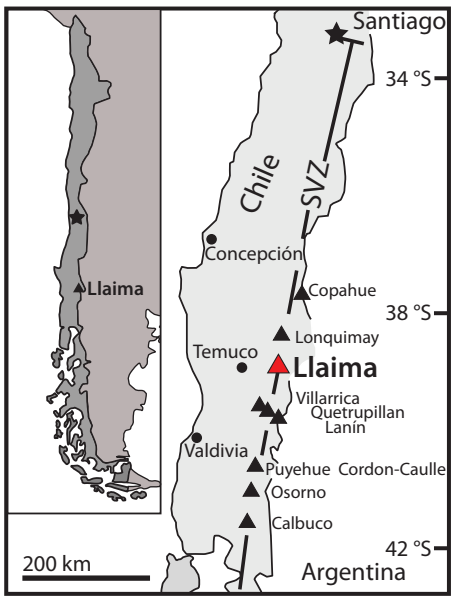

Fig. 1. Location map of Llaima within the Southern Volcanic Zone (SVZ) of the Chilean Andes (33–46°S). Shown for reference are the locations of other nearby volcanic systems; from north to south: Copahue, Lonquimay, Villarrica, Quetrupillan, Lanín, Puyehue Cordon-Caulle, Osorno, and Calbuco.

in the Rio Calbuco and Rio Captrén valleys (Global Volcanism Program, 2008) and resulted in the evacuation of the Conguillío National Park. The main explosive phase lasted ~13 h, but eruptive activity continued with reduced but intermittent Strombolian activity continuing through July 2008. A second explosive phase occurred on 3 April 2009 and the extended eruptive phase ended by July 2009. In all, the 2008–2009 eruptive phase produced lava flows extending 3 km from the vent onto the western and southern flanks, a tephra deposit with a minimum eruption volume of $1{\cdot}3 \times 10^6$ kg m^{-3} (Ruth & Calder, 2014), pyroclastic flow deposits over snow (i.e. mixed avalanches) associated with an observed vent on the (north) eastern flank, and lahars formed from the interaction of lava and the summit glacier. Retrospectively, minor increases in seismic activity and minor ash explosions were recognized in May and June 2007 but otherwise there was little or no precursory activity (OVDAS, personal communication, 2016). There is also no evidence that significant edifice deformation occurred prior to January 2008 (Fournier *et al.*, 2010; Remy *et al.*, 2015; Delgado *et al.*, in preparation).

SAMPLE COLLECTION AND PREPARATION

The tephra samples studied here are from the initial phase of the 2008 eruption, collected in January 2009 and January 2011 from a total of 94 sites in the fall deposit on the eastern flanks of the volcano (Ruth & Calder, 2014). The tephra samples were characterized in the field based on hand sample color, texture, and morphology as either black scoria, brown scoria, or plate tephra. The black scoria and plate tephra differ only in shape, and can otherwise be considered similar (Ruth & Calder, 2014). From these, 20 thin sections of representative tephra types were made for textural analysis using conventional petrography and back-scattered electron (BSE) imaging. BSE images were obtained using a Hitachi SU-70 scanning electron microscope at the University at Buffalo South Campus Instrument Center (SCIC) and the FEI Nova NanoSEM 600 in the Department of Mineral Sciences at the National Museum of Natural History (NMNH), Smithsonian Institution.

Tephra were separated by type (black and brown scoria, and plate tephra) and were lightly crushed using a jaw crusher and shaker sieved with screen sizes of 25, 40, and 80 mesh (i.e. openings of 710, 425, and 180 μm, respectively). Whole-rock analyses were conducted on the >25 mesh separate, as well as gravel-sized hand-picked samples where homogeneity could be ensured. Olivine phenocrysts were hand-picked from the 25 and 40 mesh separates of the crushed tephra.

Clear, naturally quenched, glassy melt inclusions hosted in olivine crystals were selected for analysis (see Supplementary Data for a database of melt inclusions; supplementary data are available for downloading at http://www.petrology.oxfordjournals.org) (Fig. 2). Melt inclusions containing daughter crystals were excluded. Some melt inclusions showed visible fractures but the fractures did not extend to the crystal surface. Melt inclusions contained zero to one vapor bubble. We include in the Supplementary Data the approximate location in the host olivine of the melt inclusions. Acceptable samples were mounted in epoxy in single-grain mounts to create wafered samples with the inclusions double-side exposed and polished. A total of 182 melt inclusions were analyzed.

ANALYTICAL METHODS

X-ray fluorescence

Whole-rock major elements and some trace elements (Rb, Sr, Y, Zr, V, Ni, Cr, Nb, Ga, Cu, Zn, Co, Ba, La, Ce, U, Th, Sc, Pb) for five tephra samples were analyzed by X-ray fluorescence spectrometry (XRF) with a PANanalytical 2404 system hosted at Franklin and Marshall College, Pennsylvania. Major element analyses were conducted on dried powder mixed with lithium tetraborate. The mixture was melted in a platinum crucible and then quenched into a glass disk. Total iron as Fe_2O_3 was reported from the XRF analysis and the speciation of iron was measured using titration on a separate aliquot from the crushed samples (after Reichen & Fahey, 1962). Loss on ignition was determined after samples were heated for 1 h at 950°C. The whole-rock powder was mixed with a high-purity Copolywax powder and then pressed into a briquette. Trace element analyses were conducted on these briquettes. Calibration curves were constructed with standards listed by Abbey (1983) and Govindaraju (1994). One sample was run in triplicate to determine reproducibility. For SiO_2, Al_2O_3, CaO, Na_2O the replicate analyses showed a < 1% difference; Fe_2O_3, TiO_2, MgO, and K_2O had a 1–2% difference. Replicate P_2O_5 and MnO analyses were identical.

Electron microprobe

Major element analyses of carbon-coated melt inclusions, matrix glass, plagioclase, and olivine were collected by electron microprobe analysis (EMPA) using the five-spectrometer JEOL 8900 instrument located at the National Museum of Natural History, Smithsonian Institution. Selected plagioclase and matrix glass analyses were obtained with the JEOL 8900 electron microprobe at Cornell University. Spinel inclusions in the glomerocrysts were analyzed using the five-spectrometer JEOL JXA-8430 field emission electron microprobe located at the Facilities for Analysis, Classification and Testing (FACTS) at Nanyang Technological University, Singapore. Glass analyses were collected on at least five spots per melt inclusion with a 10 μm beam diameter, 15 keV accelerating voltage, and 10 nA beam current (see Supplementary Data for details). To minimize alkali loss, we analyzed Na and K first, and for shorter on-peak durations (10 s). Our chosen wide beam diameter also minimizes alkali loss (e.g. Hayward, 2011). These techniques are

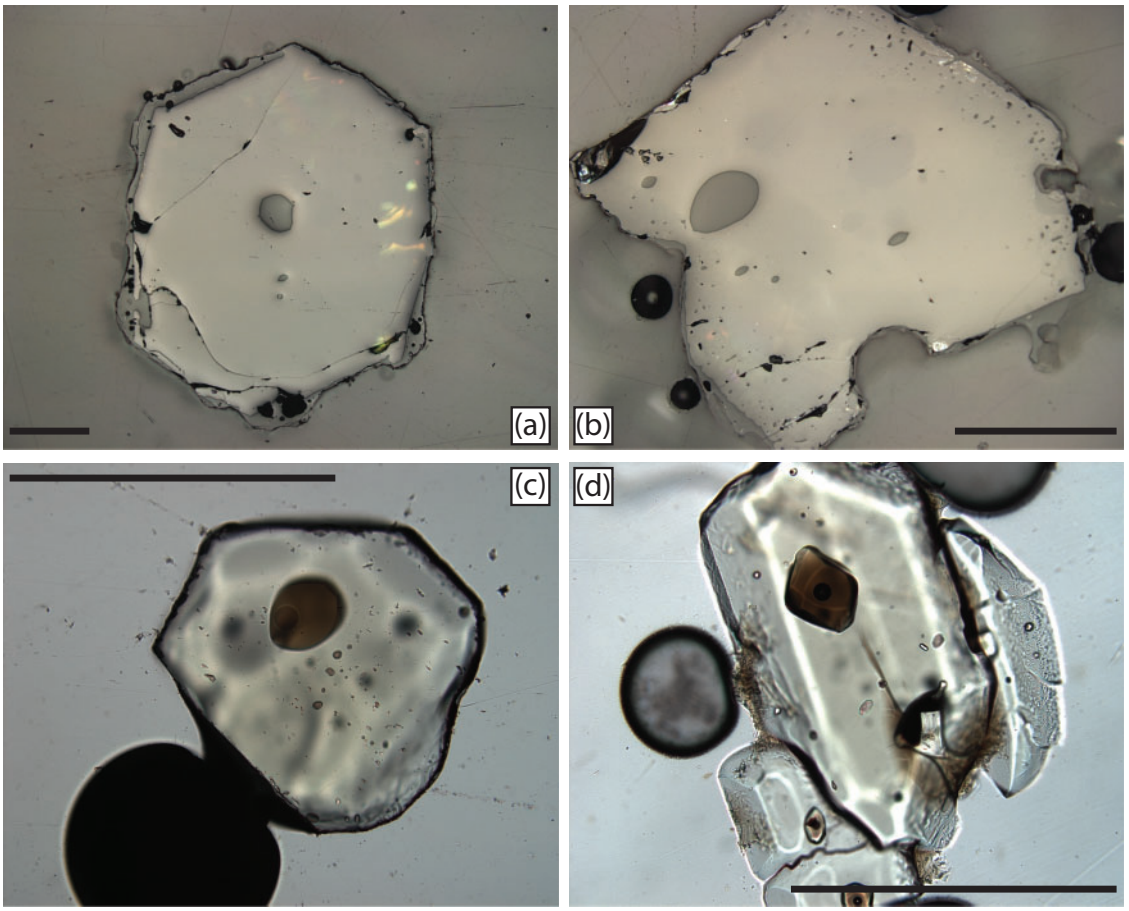

Fig. 2. A range of olivine and melt inclusion morphologies observed in the tephra samples. (a) and (b) are reflected light images whereas (c) and (d) are transmitted light images. All scale bars represent 500 μm.

reasonable as analysis of standards as unknowns (e.g. VG-2) returns Na_2O totals within 3% of reported values. Sulfur and chlorine were run after the major element analysis on a minimum of three new spots with 15 keV, 80 nA beam current, and 10 μm beam diameter. Sulfur peaks were initially obtained via a peak search routine on single melt inclusions. Because the peak position did not shift more than 2%, the peak position was determined using the search routine on scapolite during standardization. The closest (~5–10 μm from the melt inclusion) olivine probe point to the melt inclusion was considered the host olivine composition. Olivine analyses were collected with 15 keV, 40 nA beam current, and 1 μm beam diameter. Plagioclase (in thin section and the glomerocrysts) analyses were obtained with an accelerating voltage of 15 keV, 15 nA beam current, and 5 μm beam diameter. Beam conditions for the spinel analyses were 15 keV, 20 nA, and 1 μm beam diameter. For all analyses, backgrounds on each side of the peak were counted each for half the peak count times. Beam drift was assessed by running standards (glass: VG-2; plagioclase: bytownite; olivine: San Carlos olivine) as an unknown throughout the analytical run and calculating the per cent deviation from reported values.

Fourier transform infrared spectroscopy

H_2O and CO_2 concentrations were determined by Fourier transform infrared spectroscopy (FTIR) on 49 of the 182 melt inclusions using the Bio-Rad Excalibur spectrometer or the Nicolet 6700 Analytical FTIR system hosted at the National Museum of Natural History, Smithsonian Institution, following the methods of Luhr (2001). To minimize atmospheric interference on the spectra, the system (bench, microscope, and samples) was continually purged with dry, CO_2-free air. The spectral region of interest, 1000–6000 cm^{-1}, was obtained with a liquid nitrogen-cooled MCT detector, KBr beam ind splitter, and tungsten halogen source. Aperture size was selected to ideally obtain three ependent spectra per melt inclusion; they ranged from 11 μm × 22 μm to 44 μm × 44 μm. For smaller melt inclusions, the spectra measurements overlapped. Thickness data were collected with a piezometric micrometer and/or indirectly with the wavelength of fringes from 2000 to 2700 cm^{-1} (Nichols & Wysoczanski, 2007).

Water concentrations in the melt inclusions were calculated using the total H_2O peak at 3535 cm^{-1} (Stolper, 1982*a*, 1982*b*). Dissolved CO_3^{2-} concentrations were quantified using the asymmetric stretch doublet between 1515 and 1435 cm^{-1} (Dixon *et al.*, 1995). The background-corrected peak intensities were obtained

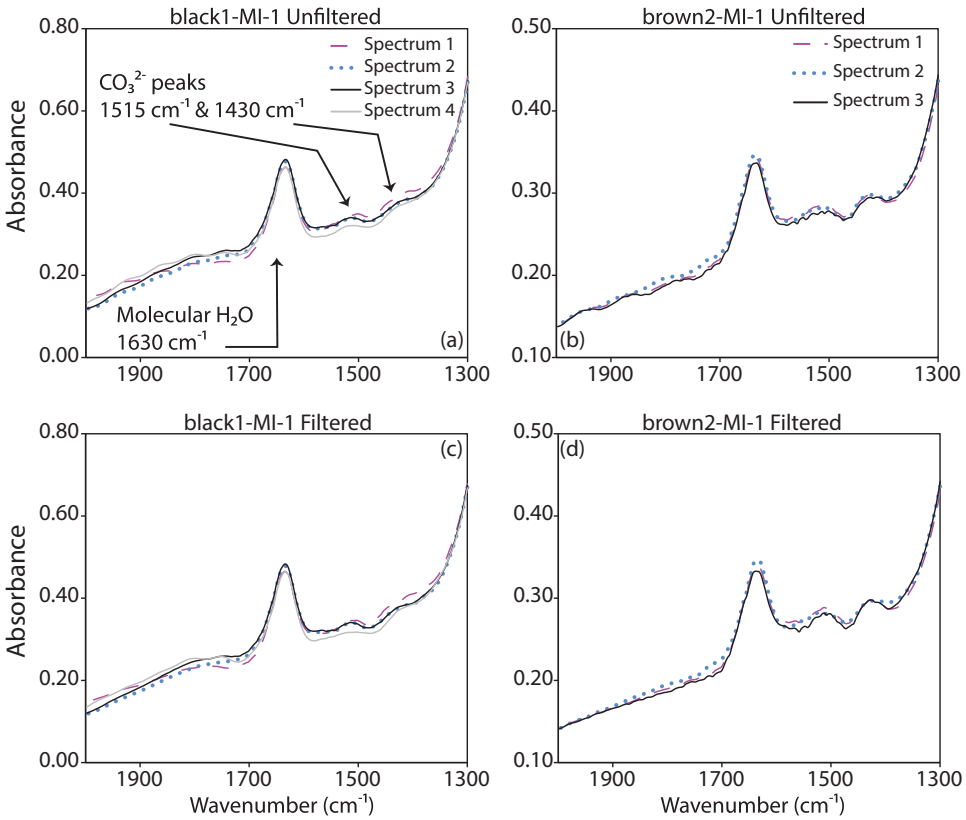

Fig. 3. FTIR spectra showing the presence of fringes and the CO_3^{2-} peaks. (a) and (b) are unfiltered data whereas (c) and (d) show the fringes-filtered spectra. There was less than 5% difference between the raw and filtered spectra, indicating that the fringes did not affect the CO_3^{2-} signal.

through an Excel fitting routine, which builds an optimized, synthetic signal that accounts for the vertical offset, the 1630 cm^{-1} total water peak, the CO_3^{2-} doublet, and a straight line (Newman *et al.*, 2000).

When fringe amplitude prevented a straightforward assessment of the intensity of the carbonate doublet, we calculated the CO_2 content of the fringe-filtered signal. The amplitude and wavelength of the fringes were modeled for each spectrum between 1800 and 2000 cm^{-1} using the curve fitting module in MATLAB (see Supplementary Data for the MATLAB script). The user imports the FTIR absorbance and wavenumber data via a Microsoft Excel file and selects a region where the script will determine the fringes' signal. The fringes' signal between 1800 and 2000 cm^{-1} can be modeled simply as a linear function overprinted by a sine function. It should be noted that this region may be overprinted by the Si–O signal from analyzed olivine (Nichols & Wysoczanski, 2007); if overprinting is present then this technique is not suitable to correct for fringes. The script fits a sine curve to the fringes, subtracts this from the original spectrum, and outputs the results into a comma-separated text file. CO_2 values were then recalculated for the fringe-subtracted signal using the Excel fitting routine described above. The difference between the fringe-filtered and unfiltered calculation is less than 5% (Fig. 3), indicating that the presence of fringes does not significantly affect the quantification of carbonate in these samples. In some cases, the CO_3^{2-} doublet was completely overwhelmed by the fringes and CO_2 values could not be reliably retrieved. The CO_2 detection limit for these melt inclusions (up to 80 μm thick) was ~400 ppm. For these samples, we report only H_2O values. In total, we performed this correction on spectra from 12 melt inclusions (see Supplementary Data for raw and fringe-corrected data).

Water was quantified using the built-in spline function in the Thermo Fischer OMNIC spectral analysis software package. Peak heights were collected on the background corrected spectra. Molar absorptivities at 1515 and 1435 cm^{-1} for C and 1635, 4500, and 5200 cm^{-1} for H species were corrected for major element composition according to Dixon *et al.* (1995). A constant value for molar absorptivity of 63 mol^{-1} cm^{-1} was applied to all 3535 cm^{-1} peaks as it is not sensitive to composition (Dixon *et al.*, 1995; Kelley & Cottrell, 2012).

Secondary ion mass spectrometry

Secondary ion mass spectrometry (SIMS) was performed on 39 additional melt inclusions because the detection limit for CO_2 by SIMS is lower (~20 ppm) than that by FTIR (~50 ppm) (Hervig *et al.*, 2003). Additional volatile analyses (H_2O, CO_2, S, Cl, F) were collected on a subset of olivine-hosted melt inclusions at the Northeast National Ion Microprobe Facility, Woods Hole Oceanographic Institution, using the Cameca IMS 1280

secondary ion mass spectrometer following the analytical procedure of Helo *et al.* (2011). These samples were polished to 0·5 μm grit (single-side only), mounted in indium, and gold-coated samples were then placed under vacuum ($<5 \times 10^{-9}$ torr) and bombarded with a 15 μm, 1·2–1·5 nA, 10 kV Cs^+ ion beam to produce the secondary ions (^{12}C, $^{16}O^1H$, ^{19}F, ^{30}Si, ^{32}S, and ^{35}Cl) with ^{30}Si as the reference mass. The samples were pre-sputtered for 4 min and the primary beam was rastered over an area of 30 μm × 30 μm. Analysis continued after pre-sputtering with an aperture reduced to 15 μm × 15 μm. Count times for $^{16}O^1H$ and ^{12}C were 10 s for 10 cycles for a total of 100 s. ^{19}F, ^{30}Si, ^{32}S, and ^{35}Cl count times were 5 s for 10 cycles for a total of 50 s. Calibration curves for measured $^{12}C/^{30}Si$, $^{16}O^1H/^{30}Si$, $^{19}F/^{30}Si$, $^{32}S/^{30}Si$, and $^{35}Cl/^{30}Si$ versus the respective volatile concentration were built from the analysis of 11 standard basaltic to andesite glasses (49–57 wt % SiO_2) (Helo *et al.*, 2011) using a York regression (see Supplementary Data for calibration curves). R^2 values were 0·99 for all volatiles measured; the reported error includes the measurement error and the error in the linear fit (see Supplementary Data).

Laser ablation inductively coupled plasma mass spectroscopy

A total of 129 melt inclusions were analyzed for 39 trace elements using laser ablation inductively coupled plasma mass spectroscopy (LA-ICP-MS). These analyses were carried out using the Thermo X-Series II quadrupole ICP-MS system coupled with a New Wave UP 213 Nd-YAG laser ablation system located at the Graduate School of Oceanography, University of Rhode Island. Spot sizes ranged from 20 to 80 μm, depending on melt inclusion size. Ablation time was maximized for the wafered samples with an energy output of 60% and 5 Hz repeat rate. Background and washout were collected for 30 s, and the maximum analytical time was 60 s. Our method was modified from that of Kelley *et al.* (2003) and Lytle *et al.* (2012). We used ^{43}Ca as an internal standard and calibrated on eight natural glasses from the USGS (BIR-1g, BHVO-2g, BCR-2g) and Max Planck Institute (GOR132-G, StHls-G, T1-G, ML3B-G, KL2-G); reference values are as reported by Kelley *et al.* (2003), Jochum *et al.* (2006), and Lytle *et al.* (2012). Acceptable linear calibration curves had $R^2 > 0{\cdot}995$ (see Supplementary Data for more information). For Ag, Pt, and W, a lower R^2 value is reported owing to limited studies on the standards used. Laboratory reproducibility is ≤5% for most trace elements.

X-ray absorption near edge structure spectroscopy (micro-XANES)

Two melt inclusions (blk3-2011 and blk1-2010) were analyzed *in situ* for $Fe^{3+}/\sum Fe$ ratios using micro X-ray absorption near edge structure (micro-XANES) spectroscopy with a precision of ±0·005 (Cottrell *et al.*, 2009). Following the methods of Cottrell *et al.* (2009), the two melt inclusions were analyzed on beamline X26a located at the National Synchrotron Light Source, Brookhaven National Laboratory. Spectra that included olivine interference were excluded (e.g. Kelley & Cottrell, 2009; Brounce *et al.*, 2014).

TEXTURAL ANALYSIS METHODS AND DEFINITIONS

Definitions

Textural analysis of crystal assemblages provides information about the kinetics of magmatic processes, especially crystallization and degassing (Hammer, 2008). We define phenocrysts here as crystals that are >100 μm and microphenocrysts as crystals that range from 30 to 100 μm. Microlites are crystals under 30 μm. Vesicles are described as rounded or convolute (i.e. irregular perimeters). Qualitative crystal shape terms used in sample characterization include acicular, tabular, swallow-tail and hopper morphologies (e.g. Lofgren, 1974; Couch *et al.*, 2003; Crabtree & Lange, 2011) (Fig. 4). Acicular crystals are characterized by needle-shape habits, whereas tabular crystals are rectangular. Swallow-tail plagioclase crystals have forked terminations, often with acicular habits. Hopper (or skeletal) morphology plagioclase crystals are those with voids often in the center (Fig. 4).

Vesicle size distributions

We measured the vesicle size distributions (VSD) to quantify the textural differences between the scoria (e.g. Polacci *et al.*, 2006; Moitra *et al.*, 2013). BSE images at 70× and 90× magnification were made binary for vesicles or crystals. Vesicle walls were manually drawn in the images in the case of breakage during sample preparation. First, we determined the phenocryst areas by manually tracing each crystal in an image; these values were subtracted from the total area measured. Then, where necessary, we reconstructed all bubble walls if portions of the septum were visible to quantify the maximum number of vesicles per image. More than 1000 vesicles were measured per thin section for two black and brown scoria samples, respectively. The vesicle data obtained include area, major axis, minor axis, and perimeter. Equivalent radius and diameter were calculated from the area values. Because we are interested in an internal comparison, here we report 2D values to avoid complications owing to stereological conversion (Polacci *et al.*, 2006).

Crystal size distributions

We used BSE images to collect crystal size data for plagioclase crystals from the brown and black scoria. Long and short axes were measured using ImageJ freeware (http://rsb.info.nih.gov/ij/). We estimated crystal aspect ratios using the CSDSlice technique (Morgan & Jerram, 2006) and considered the textural fabric as massive; we did not correct for crystal roundness. Using petrography and built-in features within ImageJ,

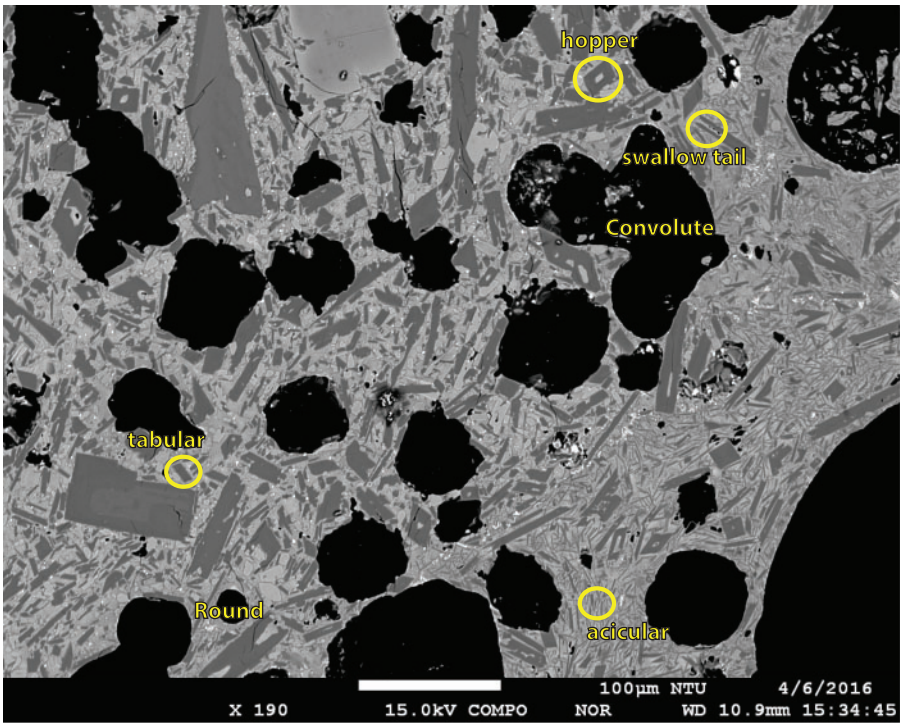

Fig. 4. An example backscattered electron image of black scoria, highlighting specific plagioclase and vesicle textural features discussed in this study. With respect to plagioclase, we show hopper, swallow-tail, tabular, and acicular morphologies. We highlight round and convolute vesicles.

we determined the total slide area, volumetric phase abundance, and vesicularity. With these data we calculated the crystal size distributions (CSD) of the plagioclase using the software CSD Corrections 1.51 (http://www.uqac.ca/mhiggins/csdcorrections.html) after Higgins (2006). Higgins (2000) reported maximum errors of ± 0·5 ln units in the population density.

PETROGRAPHIC RESULTS

Scoria textures

The black scoria usually occurs as sub-angular lapilli, although flatter examples (i.e. 'plate tephra'; Ruth & Calder, 2014) are common in the proximal (<9 km) deposit. The brown scoria occurs only as sub-angular, highly vesicular lapilli. General crystallinity (groundmass + phenocrysts) for the black scoria is between 50 and 60 vol. %, whereas the brown scoria crystallinity ranges from 10 to 15 vol. % (Ruth & Calder, 2014). Average vesicularity for both scoria types was derived from density measurements (after Houghton & Wilson, 1989). Black scoria vesicles tend to be large and convoluted, with an average vesicularity of 79%. Conversely, vesicles in the brown scoria tend to be smaller and rounder, with an average vesicularity of 88% (Ruth & Calder, 2014).

The phenocryst phase assemblage is plagioclase (~1–2 vol. % in brown scoria, 4–7 vol. % in black scoria), olivine (<1 vol. % in both scoria types), rare titanomagnetite and orthopyroxene (≪ 1 vol. %). Plagioclase is the dominant mineral in the groundmass and is found in all scoria types. Titanomagnetite and orthopyroxene are present as groundmass phases in the black scoria, but are rarely observed in the brown scoria.

Plagioclase phenocrysts show significant signs of disequilibrium including sieve textures and compositional zoning [also observed by Bouvet de Maisonneuve *et al.* (2012*b*)]. Some plagioclase phenocrysts show additional features such as dendrite-like or swallow-tail terminations (Fig. 5a). Plagioclase microphenocrysts have an euhedral, tabular crystal habit and instances of hollow cores, hopper shapes, and minor swallow-tail terminations. They show little to no sieve texture and are sometimes normally zoned; these are found only in the black scoria.

A wide range of microlite morphologies is observed in the black scoria, in which habits range from tabular to acicular, often in an interlocking configuration (Fig. 5b). Within the brown scoria, microlite habits are dominantly acicular, although tabular microlites are sometimes observed. Crystal-free matrix glass is limited within the black scoria, whereas it is more abundant in the brown scoria (Fig. 5c). Additionally, microlite-rich textural domains, similar to the black scoria, are present in the brown scoria (Fig. 5d). Late-stage oxide microlites exhibiting cruciform habits are often found along the boundary separating the two textural domains (Ruth & Calder, 2014). Additional images are provided in the Supplementary Data. A summary of the textural features of the brown and black scoria is given in Table 1.

Plagioclase and olivine (i.e. troctolite) glomerocryst clusters are also present in all tephra. They are subdivided into two groups based on textural features and

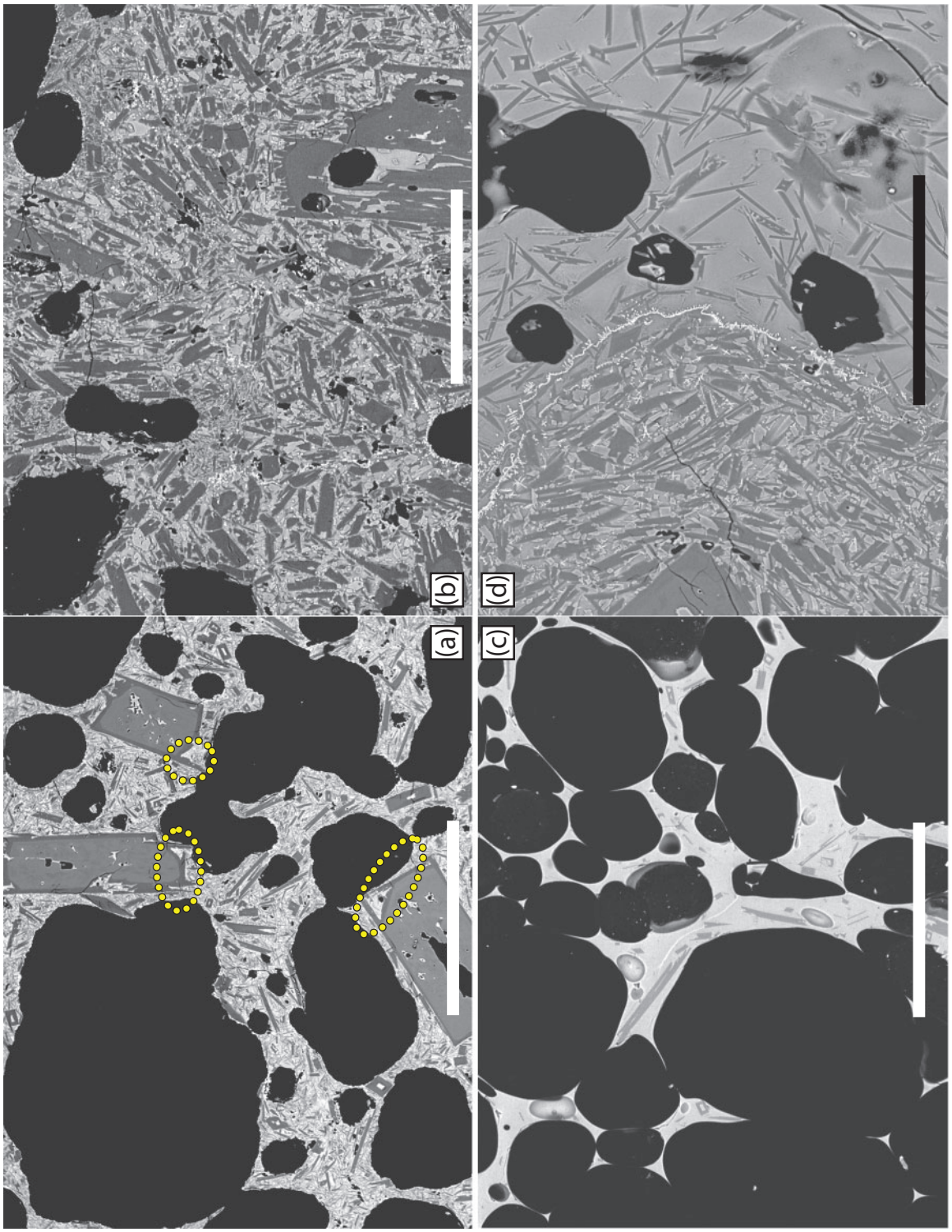

Fig. 5. Backscattered electron images of the textural features of black and brown scoria. (a) and (b) show the microlite textures found in black scoria. In (a) there are abundant acicular plagioclase microlites (dark gray) alongside microphenocrysts and phenocrysts. The circled plagioclase phenocrysts show skeletal growths. In (b) the plagioclase microlites are dominantly tabular in morphology. (c) The textural features of brown scoria, which shows less abundant acicular microlites and abundant vesicles. (d) The distinct boundary between two textural domains found in brown scoria. The boundary is highlighted by spinel with cruciform morphology, suggesting rapid growth. The scale bar represents 100 μm.

Table 1: Summary table of crystalline and vesicle textures observed in the brown scoria and black lapilli scoria

	Vesicles	Crystallinity (phenocrysts + groundmass)	Phenocrysts	Micro-phenocrysts	Microlites	Matrix glass	Other
Black scoria	79% convolute	50–60 vol. %	4–7 vol. % plg, ol	plg: normally zoned, pristine	plg: tabular and acicular, interlocking configuration	Limited	
Brown scoria	88%, round	10–15 vol. %	1–2 vol. % plg, ol	Rarely observed	plg: acicular, sometimes tabular	Abundant	Domains with black scoria textures

Textural information on the black plate tephra has been given by Ruth & Calder (2014).

mineralogy (Fig. 6). One suite of glomerocrysts shows anhedral equigranular plagioclase and olivine with limited amounts of matrix glass containing round vesicles (Fig. 6a). The plagioclase phenocrysts are minimally sieve-textured. Subhedral to euhedral spinel grains are observed as inclusions in pristine plagioclase and olivine crystals; these are hereafter referred to as Cr-spinel troctolite glomerocrysts. In the other suite of glomerocrysts, the plagioclase phenocrysts show significant sieve textures, the olivine phenocrysts are much smaller and less abundant, matrix glass is generally more abundant with convolute and round vesicles, and the spinel phase is rare (Fig. 6b). These are referred to as Cr-spinel-free troctolite glomerocrysts. Cr-spinel troctolite glomerocrysts are generally found in the brown scoria, whereas the Cr-spinel-free troctolite glomerocrysts are found in the brown and black scoria. The glomerocrysts were noted but not studied by Bouvet de Maisonneuve *et al.* (2012*a*), and were thought to originate from a crystal mush. This inference is reasonable given that the glomerocrysts' mineral chemistry is similar to that of the scoria. Additionally, it is unlikely that they are assimilated country rock given that the underlying basement comprises evolved Tertiary intrusive rocks (Lucassen *et al.*, 2004).

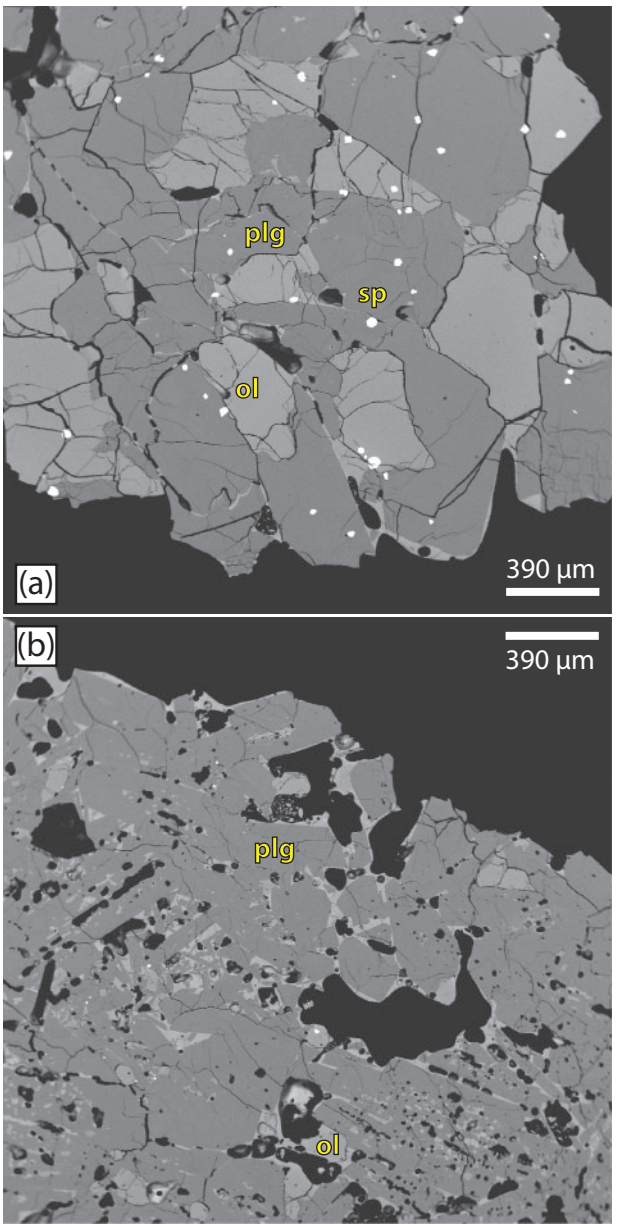

Fig. 6. Backscattered electron images of plagioclase–olivine glomerocrysts. The bright phase is spinel, the medium gray phase is olivine, and the dark phase is plagioclase. (a) Cr-spinel troctolite glomerocryst in equilibrium with olivine and spinel. It should be noted that there are a few vesicles in the surrounding matrix glass. (b) Cr-spinel-free troctolite glomerocryst with significantly less olivine and no spinel present.

Crystal and vesicle size distributions

Results from the vesicle textural analysis are shown in Table 2. Vesicle number densities are similar for the brown scoria samples (e.g. 124 and 142), whereas the black scoria samples exhibit higher and lower values (e.g. 106 and 166). The larger vesicle number density value for 1Black is puzzling given that the crystallinity and vesicularity are distinctly different from those of the brown scoria (see below). One explanation is that the textures could reflect mingling of magma at different textural stages (e.g. Lautze & Houghton, 2007). The black scoria have a larger average vesicle diameter (0·074 mm) and a wider range of vesicle sizes (<0·01 to 1·74 mm), whereas vesicles in the brown scoria are smaller (0·044–0·055 mm) and are characterized by narrower range of sizes (<0·01 to 0·4 mm) (Fig. 7). The black and brown scoria have broadly similar VSD with linear segments (Fig. 7), indicative of steady-state nucleation and growth (Mangan & Cashman, 1996). However, the VSD of the black scoria diverges from that of the brown scoria at around 0·1 mm (see Fig. 7 inset), and is characterized by

Table 2: Textural input and output for vesicle size distribution measurements

Sample	Total area measured (mm^2)	Phenocryst area (mm^2)	Total area – phenocryst area	Number of vesicles measured	VND (mm^{-2})	Average diameter (mm)	SD (mm)
Brown	18·8	0·2	18·6	2315	124	0·055066	0·058757
brown	9·1	0·2	8·9	1260	142	0·044447	0·052181
1Black	13·7	0·6	13·0	2162	166	0·074175	0·155396
2Black	19·6	1·4	18·2	1935	106	0·074638	0·1865

Average diameter $= 2$[area fraction/($\pi \times$ vesicle number density)]$^{1/2}$.

a lower slope, indicative of longer growth rates. The brown scoria shows a small plateau in the smallest vesicle diameters, which may reflect the initial stages of vesicle ripening (Mangan & Cashman, 1996).

The statistical summary for the plagioclase crystal size data is presented in Table 3. Crystal number density (CND), the number of crystals per unit area, generally decreases from the black scoria (including plate tephra for comparison) to brown scoria. Sample BrownLL has an exceptionally large CND and the average crystal size for this sample ($\sim$4 μm) is almost half the average for the other brown scoria (7 and 9 μm). The black and brown scoria have generally concave-up crystal size distributions (CSD), whereas the plate tephra have a kinked profile (Fig. 8). The plate tephra have a significant component of larger crystal sizes, which manifests as another kink in the CSD; it is unclear to what extent this might be a sampling artifact. However, the plate tephra formed from ruptured bubble films, probably from magma that resided near the conduit margins (Ruth & Calder, 2014). Magma near the conduit margins probably had the longest residence times, thus producing the highest crystallinities and largest crystals. One sample of brown tephra, brn1, exhibits textures similar to that of the black scoria, which could suggest that it is a transitional texture. The concave-up distribution has been attributed to super-exponential nucleation events (i.e. growth rate is a function of crystal size; Marsh, 1998) whereas a kinked profile is commonly observed in igneous systems and interpreted as a signature of magma mixing (Marsh, 1998; Higgins, 2006; Vinet & Higgins, 2010). Overall, the slope decreases from the brown to black scoria and plate tephra. Similarly, plot intercepts decrease slightly from the brown to black scoria and plate tephra (see Fig. 8 insets). Changes in slope can be attributed to increased residence time and/or coarsening (Higgins, 2006). Plot intercepts are not expected to change with increased residence time; however, they do decrease with coarsening (Vinet & Higgins, 2010). BrownLL has the highest intercept of all the tephra, which, combined with the high crystal number density, suggests a rapid nucleation event. Since the plot intercepts decrease in these datasets, the change in slope might result from coarsening via Ostwald ripening. Both plate tephra samples and one black scoria (1Black) sample show a kink in their CSD at the smallest crystal sizes, which is not observed in the brown or black scoria. This extra kink could suggest that these samples may have experienced coarsening with a nucleation event just before eruption. Similar distributions and interpretations were presented theoretically (Marsh, 1998) and for samples from Soufrière Hills volcano (Higgins & Roberge, 2003).

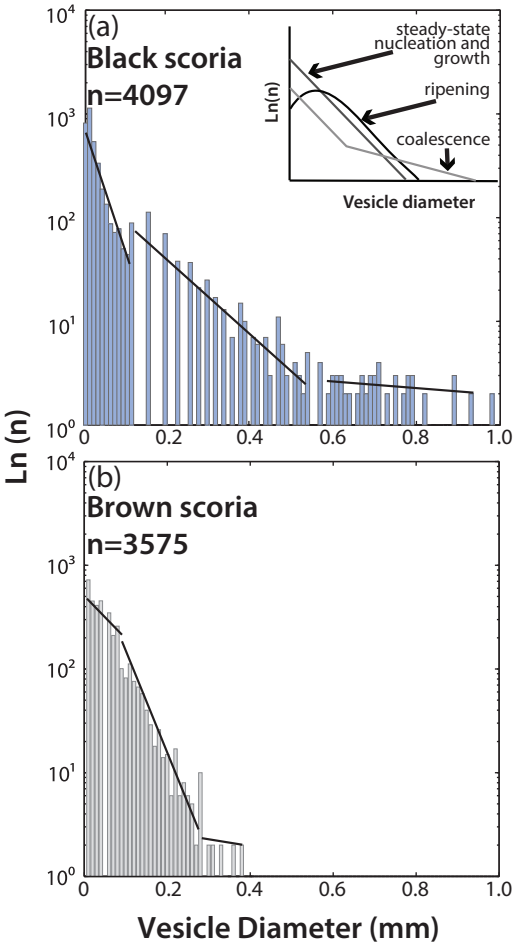

Fig. 7. Vesicle size distribution histograms for (a) black and (b) brown scoria. Inset figure in (a) shows interpretative models of different vesicle size histograms (after Mangan & Cashman, 1996). The lines on the histograms denote the approximate slope of each section. The small plateaux in the small vesicle sizes in the brown scoria are indicative of vesicle ripening (Mangan & Cashman, 1996). The black scoria exhibit two linear segments; this feature suggests coalescence and residence.

GEOCHEMICAL RESULTS

Whole-rock major elements

The whole-rock composition of the tephra produced during the 2008 eruption is basaltic with $\sim$51 wt % of SiO_2 ($n = 5$ whole-rock samples), consistent with

Table 3: Textural inputs for crystal size distribution measurements

Sample	Total area (mm^2)	Total bubbles area (mm^2)	% Bubbles	Major axis	Intermediate axis	Minor axis	No. of crystals measured	CND
Brown	14·1374	10·41910152	73·7	2	1	1	5487	1476
Brown1	16·1369	11·8370804	73·4	2	1	1	5893	1371
BrownLL	1·5206	0·77426498	50·9	1·15	1·05	1	7485	10029
Black	6·9795	2·74364145	39·3	2	1	1	9298	2195
1Black	3·4565	1·72197592	49·8	10	1	1	8636	4979
2Black	7·511	3·7982712	50·6	2	1	1	9279	2499
Plate	2·2893	0·41159049	18	10	1	1	7917	4216
Plate3	3·7005	0·2743954	7·4	10	1	1	7332	2140

CND, crystal number density; the number of crystals per unit area.

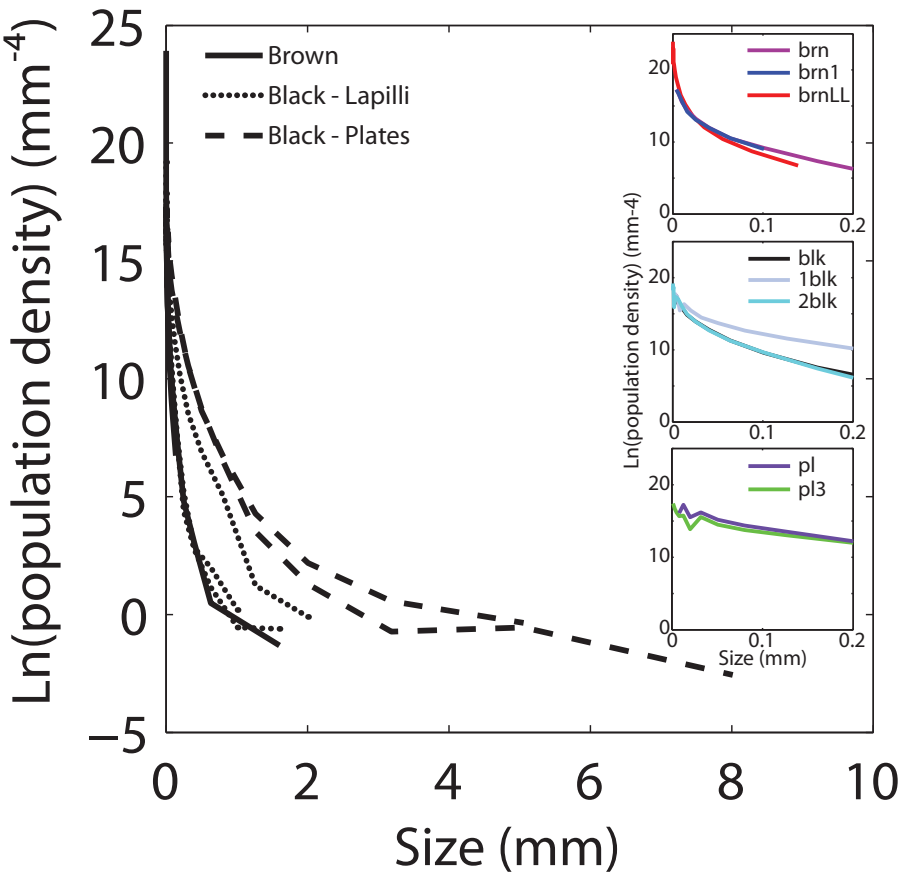

Fig. 8. Crystal size distributions for the tephra erupted during the explosive phase. The insets show the breakdown by tephra type and sample. The decrease in slope from brown to black scoria to plates, and the decrease in *y*-intercept from brown to black scoria to plates, should be noted.

previously reported whole-rock chemistry from recent Llaima products (Naranjo & Moreno, 2005; Reubi *et al.*, 2011; Bouvet de Maisonneuve *et al.*, 2012*a*). These and additional geochemical data are provided in the Supplementary Data. The black scoria samples have SiO_2 values of 51·2–51·59 wt %; brown scoria samples have similar SiO_2 values, at 51·20–51·22 wt %. These data suggest, unlike the textural data, that there is no discernible geochemical difference in whole-rock chemistry between the black and brown scoria. This finding is consistent with texturally bimodal tephra reported elsewhere (e.g. Cimarelli *et al.*, 2010; Métrich *et al.*, 2010).

Phenocryst major elements

Mineral chemistry was determined on the phenocryst phases, the plagioclase microphenocrysts, and all phases in the glomerocrysts (Table 4). The composition of the isolated plagioclase phenocrysts and microphenocrysts is in the range of $An_{85–65}$, with an average of An_{69} (Fig. 9). Isolated olivine phenocryst compositions are in the range of $Fo_{83–66}$. Plagioclase within the Cr-spinel-free troctolite glomerocrysts is in the range of $An_{92–65}$, whereas the plagioclase in the Cr-spinel troctolite glomerocrysts is slightly more calcic at $An_{92–75}$. Olivine composition within both types of glomerocrysts clusters around Fo_{81}. Zoning information is limited to a small subset ($n = 14$) of olivine

Table 4: Representative mineral analyses (olivine, plagioclase, spinel) obtained with the electron microprobe

Type:	BRN3-1-2010 Host ol	bk2-5-1-2012 Host ol	br3-1-1-2012 Host ol	br4-2-2-2012 Host ol	3 blk_ol_2-52 Glom. ol	15 brn_ol_3-199 Glom. ol	7 blk_ol_6-128 Glom. ol	6 blk_ol_5-95 Glom. ol
SiO_2	36·41	38·74	39·67	40·21	37·67	40·59	39·24	37·67
TiO_2	n.d.	0·05	0·01	0·01	n.d.	n.d.	n.d.	n.d.
Al_2O_3	n.d.	0·02	0·01	0·02	n.d.	n.d.	n.d.	n.d.
Cr_2O_3	0·00	0·01	0·02	0·02	0·01	0·02	0·02	0·01
FeO	30·14	21·24	18·02	14·99	19·09	17·24	16·97	16·99
MnO	0·49	0·33	0·27	0·22	0·31	0·27	0·27	0·27
MgO	33·74	39·23	42·07	44·88	40·90	40·76	42·73	46·10
NiO	0·07	0·11	0·13	0·20	0·11	0·15	0·16	0·12
CaO	0·27	0·22	0·19	0·18	0·22	0·20	0·20	0·25
Total	101·11	99·94	100·38	100·72	98·32	99·22	99·60	101·40
Si	0·98	1·00	1·01	1·00	0·99	1·03	1·00	0·95
Ti	n.d.	0·00	0·00	0·00	n.d.	n.d.	n.d.	n.d.
Al	n.d.	0·00	0·00	0·00	n.d.	n.d.	n.d.	n.d.
Cr	0·00	0·00	0·00	0·00	0·00	0·00	0·00	0·00
Fe^{2+}	0·68	0·46	0·38	0·31	0·42	0·37	0·36	0·36
Mn	0·01	0·01	0·01	0·00	0·01	0·01	0·01	0·01
Mg	1·35	1·51	1·59	1·67	1·60	1·55	1·62	1·73
Ni	0·00	0·00	0·00	0·00	0·00	0·00	0·00	0·00
Ca	0·01	0·01	0·01	0·00	0·01	0·01	0·01	0·01
∑Cation	3·02	3·00	2·99	3·00	3·01	2·97	3·00	3·05
%Fo	66·25	76·42	80·39	84·03	78·98	80·58	81·54	82·64

Type:	13 brn_plg_3-236 Glom. plag	15 brn_plg_5-269 Glom. plag	Black-655 Scoria plag	WAQ-738 Scoria plag	WAQ-737 Scoria plag	Black-657 Scoria plag	Black-656 Scoria plag	ZRN-732 Scoria plag
SiO_2	44·46	44·07	53·75	52·52	52·57	52·18	49·38	47·70
TiO_2	0·03	0·00	0·036	0·175	0·068	0·036	0·007	0·018
Al_2O_3	33·95	34·39	28·75	29·11	29·89	30·00	32·56	32·81
FeO	0·57	0·54	1·22	1·08	0·92	0·84	0·95	0·58
MgO	0·07	0·07	0·31	0·33	0·26	0·26	0·30	0·12
CaO	18·08	18·39	11·80	12·24	13·21	13·54	13·08	16·85
Na_2O	1·09	0·87	4·24	4·14	3·87	3·74	3·32	2·01
K_2O	0·02	0·01	0·17	0·16	0·12	0·07	0·11	0·02
Total	98·27	98·34	100·28	99·75	100·90	100·67	99·70	100·11
Si	2·09	2·08	2·43	2·40	2·37	2·36	2·26	2·19
Ti	0·00	0·00	0·00	0·01	0·00	0·00	0·00	0·00
Al	1·88	1·91	1·53	1·56	1·59	1·60	1·76	1·78
Fe^{2+}	0·02	0·02	0·05	0·04	0·03	0·03	0·04	0·02
Mg	0·00	0·01	0·02	0·02	0·02	0·02	0·02	0·01
Ca	0·91	0·93	0·57	0·60	0·64	0·66	0·64	0·83
Na	0·10	0·08	0·37	0·37	0·34	0·33	0·29	0·18
K	0·00	0·00	0·01	0·01	0·01	0·00	0·01	0·00
∑Cation	5·02	5·02	4·99	5·00	5·00	5·00	5·01	5·01
%An	90·07	92·05	59·97	61·41	64·90	66·42	68·05	82·18

Type:	17 Llaima5-287 oxide	18 Llaima6-294 oxide	18 Llaima7-295 oxide	19 Llaima7-296 oxide	20 Llaima8-301 oxide	21 Llaima9-304 oxide	24 Llaima12-311 oxide
SiO_2	0·08	0·10	0·11	0·20	0·16	0·05	0·11
TiO_2	0·61	1·25	1·25	0·63	1·40	1·03	1·46
Al_2O_3	31·19	27·79	27·29	32·94	20·80	27·52	21·87
Cr_2O_3	23·06	22·50	22·84	22·99	27·28	23·41	25·57
FeO	29·80	36·23	36·89	29·83	39·07	35·92	39·70
MnO	0·19	0·23	0·19	0·16	0·23	0·19	0·24
MgO	14·51	12·74	12·68	14·59	10·18	12·94	10·99
CaO	0·24	0·21	0·16	0·20	0·37	0·12	0·26
Total	99·69	101·05	101·40	101·53	99·49	101·18	100·20
Si	0·00	0·00	0·00	0·00	0·00	0·01	0·00
Ti	0·03	0·03	0·03	0·03	0·07	0·01	0·03
Al	0·94	0·86	0·79	0·74	0·53	1·11	0·77
Cr	0·55	0·60	0·62	0·73	0·66	0·52	0·68
Fe^{3+}*	0·46	0·48	0·52	0·48	0·66	0·34	0·51
Fe^{2+}*	0·45	0·48	0·50	0·50	0·60	0·37	0·52
Mn	0·01	0·01	0·01	0·01	0·01	0·00	0·01
Mg	0·55	0·53	0·51	0·50	0·46	0·62	0·48
Ni	0·00	0·00	0·00	0·00	0·00	0·00	0·00
∑Cation	2·99	3·00	2·99	2·99	3·00	2·99	2·99
Cr#	28·31	30·87	32·10	37·27	35·86	26·38	34·68

n.d., not determined.
*Fe^{2+} and Fe^{3+} determined through charge balancing.

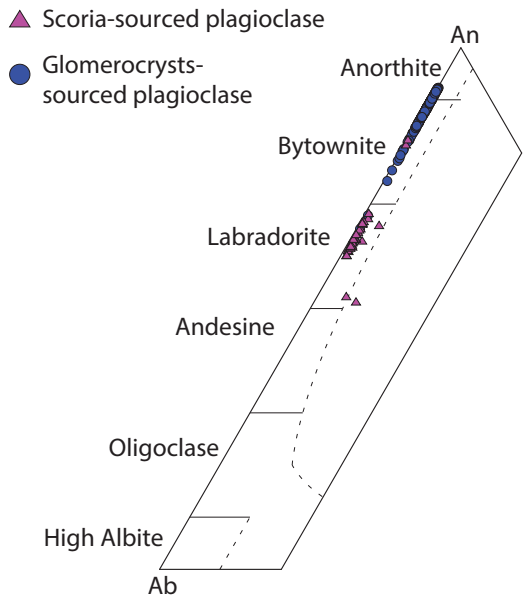

Fig. 9. Modified plagioclase ternary diagram following the disordered feldspar classification scheme of Deer *et al.* (1992). The triangles denote scoria-sourced microphenocryst plagioclase whereas the circles are plagioclases found in the glomerocrysts.

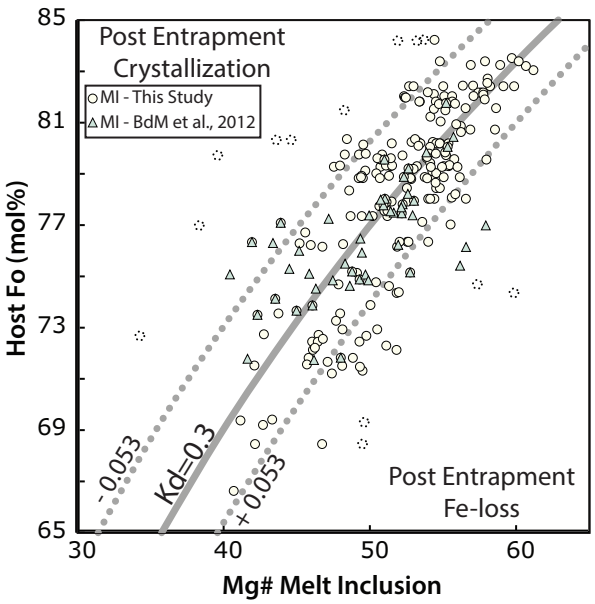

Fig. 10. Rhodes diagram of Fo (mol %) of the host olivine versus the Mg# of melt inclusions, after Dungan *et al.* (1978) and Rhodes *et al.* (1979). Samples are plotted assuming NNO, and Fe_2O_3 is 20% of the total Fe (Cervantes & Wallace, 2003). Samples in the top left have experienced post-entrapment crystallization, whereas those in the lower right have experienced Fe loss. The bold gray curve shows equilibrium, which equates to $K_D = 0{\cdot}3$. The gray dotted lines are acceptable deviations from equilibrium (Putirka, 2008). The circles are melt inclusion analyses from this study whereas the triangles are analyses from the literature (Bouvet de Maisonneuve *et al.*, 2012*a*; abbreviated as BdM *et al.* 2012a). The dotted circles represent samples that were subsequently eliminated from further study because of likely post-entrapment modifications.

crystals; these are dominantly reversed zoned, which is consistent with previously reported observations (Bouvet de Maisonneuve *et al.*, 2012*a*). The spinel phase is Cr- and Al-rich with Cr# [molar Cr/(Cr + Al + Fe^{3+})] ranging from 26 to 37. Cr-spinel in conjunction with high-An plagioclase is consistent with origins in the deeper part of the magmatic plumbing system (e.g. Streck *et al.*, 2002). Conversely, the lack of spinel and slightly lower An plagioclase in the Cr-spinel-free troctolite glomerocrysts is consistent with origins in the shallower parts of the plumbing system.

Post-entrapment modification of melt inclusions and Fe oxidation state

Melt inclusions may experience compositional modification after trapping. Processes may include crystallization, melting, re-equilibration with the host mineral, and elemental diffusion through the host mineral [for a review see Kent (2008)]. To undertake meaningful analysis of the data, estimating the extent of these modifications is important.

Post-entrapment modifications through Fe loss or crystallization were determined by comparing the Fe–Mg exchange coefficients (K_D) of the melt inclusion and host olivine (Putirka, 2008) (Fig. 10). Melt inclusion compositions were corrected for post-entrapment crystallization by adding host olivine in 0·01% increments until $K_D(Fe^{2+}\text{–}Mg)^{ol\text{–}liq} = 0{\cdot}3$ (Roeder & Emslie, 1970) using the Ford *et al.* (1983) olivine–melt model in the PETROLOG 3 software package (Danyushevsky & Plechov, 2011). $Fe^{3+}/\sum Fe$ ratios were measured via XANES on two melt inclusions; blk3-2011 yielded 0·194 ± 0·002 whereas blk1-2010 gave a value of 0·163. These values were used for post-entrapment corrections for these samples. For samples that were not analyzed with XANES, our post-entrapment crystallization (PEC) corrections assumed an oxygen fugacity equivalent to the nickel–nickel oxide (NNO) oxygen buffer typical of arc systems (Toplis & Carroll, 1995) and an $Fe^{3+}/\sum Fe$ ratio of 0·2, based on literature values for other arc systems (e.g. Cervantes & Wallace, 2003; Lloyd *et al.*, 2013). We tested this assumption using equation (7) from Kress & Carmichael (1991) to estimate the oxygen fugacity buffer with a range of $Fe^{3+}/\sum Fe$ values (Table 5). When 20% Fe is Fe_2O_3, the buffer is ΔNNO +0·06 to + 0·14 for the samples shown. At $Fe^{3+}/\sum Fe$ = 15%, the buffer is much closer to ΔNNO (–0·72 to –0·63), or ΔQFM (where QFM is the quartz–fayalite–magnetite buffer). The buffer did not change considerably with changing pressures in the model. Under this assumption, most samples experienced <10% post-entrapment crystallization.

We assessed Fe loss to the host crystal (e.g. Danyushevksy *et al.*, 2000) by comparing the FeO* and Mg# of the melt inclusions (anhydrous, normalized data) with the FeO* and Mg# trend of whole-rock samples (Fig. 11). Melt inclusion compositions are consistent with the whole-rock array, but extend to significantly more mafic compositions. Four samples showed evidence of post-entrapment Fe loss. These

Table 5: Oxygen fugacity calculations using equation (7) from Kress & Carmichael (1991)

Sample:	BLK1-1-2010	blk3-MI-1-2011	blk8-MI-1-2011	brn8-MI-1-2011
SiO_2	52·04	53·09	51·68	50·93
TiO_2	1·01	1·55	0·92	1·06
Al_2O_3	15·74	12·89	16·95	16·96
FeO*	9·38	11·01	9·81	9·11
MnO	0·20	0·19	0·16	0·15
MgO	4·16	5·35	4·81	5·44
CaO	8·76	7·48	9·02	9·02
Na_2O	3·29	3·04	3·24	3·33
K_2O	0·64	1·04	0·49	0·60
P_2O_5	0·27	0·29	0·15	0·19
Sum	95·48	95·94	97·23	96·79
T (°C)	1147	1188	1131	1152
P (MPa)	50	50	50	50
$Fe^{3+}/\sum Fe$	0·15	0·15	0·15	0·15
ΔNNO	−0·72	−0·63	−0·66	−0·71
$Fe^{3+}/\sum Fe$	0·20	0·20	0·20	0·20
ΔNNO	+0·06	+0·14	+0·12	+0·07
$Fe^{3+}/\sum Fe$	0·25	0·25	0·25	0·25
ΔNNO	+0·693	+0·779	+0·75	+0·71

All calculations are at the given pressure and temperature.

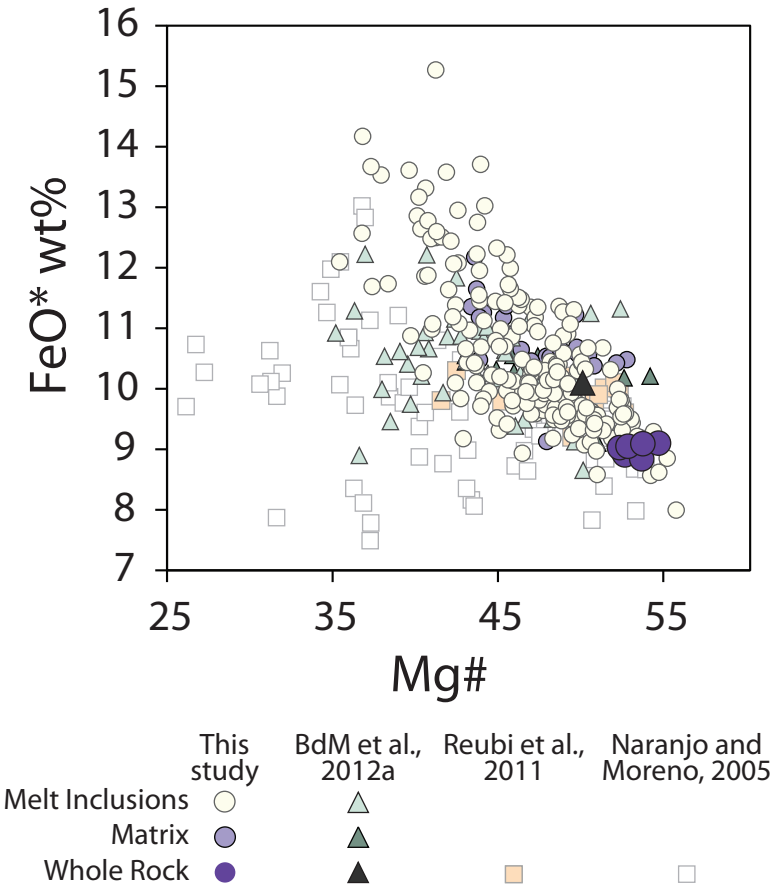

Fig. 11. FeO* (total from EMPA) vs Mg# of the melt inclusions. Also plotted are the matrix glass, and whole-rock analyses from this study, and from Bouvet de Maisonneuve *et al.* (2012*a*) (abbreviated as BdM *et al.* 2012a), Reubi *et al.* (2011), and Naranjo and Moreno (2005). If the melt inclusions plot along the same trend as the whole-rock values then Fe loss can be considered minimal.

inclusions were all less than 40 μm, considerably smaller than other melt inclusions in the suite, which ranged from <20 to 425 μm in diameter (average 68 μm). As such, they could re-equilibrate faster than larger melt inclusions and, therefore, their measured compositions may not reflect actual magmatic compositions (Cottrell *et al.*, 2002). Because of well documented post-entrapment complications from Fe loss (e.g.

Danyushevsky *et al.*, 2000), these melt inclusions were filtered from the suite.

Water concentrations in olivine-hosted melt inclusions may be affected by post-entrapment diffusion of H, and possibly molecular water, through the olivine crystal lattice (Johnson *et al.*, 2008; Métrich & Wallace, 2008; Portnyagin *et al.*, 2008). Three lines of evidence argue against significant diffusive water loss from the majority of our inclusions. First, significant water loss may cause extensive (>10%) post-entrapment olivine crystallization by increasing the inclusion liquidus temperature (Bucholz *et al.*, 2013; Lloyd *et al.*, 2013). We therefore do not include any inclusions with >10% post-entrapment crystallization in this study. Second, H loss may initiate precipitation of fine magnetite within the melt inclusion (Danyushevsky *et al.*, 2002; Métrich & Wallace, 2008), although this has been contested in other studies, which have proposed that proton diffusion into the inclusion is rapid and would mitigate any changes in oxidation state (Gaetani *et al.*, 2012; Bucholz *et al.*, 2013). We do not include any inclusions with daughter crystals in this study. Third, comparisons of olivine-hosted melt inclusions sourced from ash, lapilli, and bombs show that samples sourced from lapilli, such as those we report on here, may experience limited amounts of water diffusion (Lloyd *et al.*, 2013). We consider diffusive water loss minimal, although it cannot be entirely excluded. In summary, in the subsequent discussion we consider only glassy melt inclusions that are free of daughter crystals, although vapor bubbles may be present, are without significant Fe loss, and have less than 10% post-entrapment crystallization.

Recent studies have shown that CO_2 concentrations in melt inclusions are also altered by post-entrapment processes (e.g. Neave *et al.*, 2014; Wallace *et al.*, 2015; Aster *et al.*, 2016). In particular, post-entrapment modifications of the melt inclusion via cooling and crystallization cause a decrease in pressure. CO_2 partitions into the resultant vapor bubble because of the pressure dependence of its solubility. This can be augmented if there is H^+ loss via diffusion into the host mineral. Ultimately, these processes lower the CO_2 content of the melt inclusion by as much as 40–90% (Wallace *et al.*, 2015; Aster *et al.*, 2016). Recovering the original CO_2 contents of the melt inclusion requires knowing the volume of the vapor bubble and the CO_2 density within the bubble; however, we do not have these data for our suite of inclusions. Alternatively, original melt inclusion CO_2 contents may be estimated assuming that a bubble forms during thermal contraction associated with crystallization and cooling (Aster *et al.*, 2016); the bubble volume can be estimated with crystallization and thermal contraction models. However, this correction assumes that the olivines have higher entrapment temperatures than eruption temperatures. Of the 182 melt inclusions analyzed in this study, entrapment temperatures were lower than eruption temperatures for 171 melt inclusions [calculated using the technique outlined by Aster *et al.* (2016)]. These melt inclusions are less likely to have experienced thermal contraction. This suggests that the Aster *et al.* (2016) protocol may not be appropriate for these samples. We report uncorrected CO_2 values and consider these as minima.

Major elements in melt inclusions

Our melt inclusion dataset shows a wide compositional range, with the most mafic and most evolved compositions being 49 and 56 wt % SiO_2 respectively, expanding on the previously reported compositional range (Bouvet de Maisonneuve *et al.*, 2012*a*) (Table 6). The matrix glasses show similar trends to the melt inclusions, but with a smaller range of values for all elements (e.g. 52–55 wt % SiO_2). The majority of the samples (152 of 182 melt inclusions) are consistent with a single liquid line of descent (LLD) involving fractionation of olivine and plagioclase (Fig. 12). The CaO and Al_2O_3 trends do not change slope with respect to SiO_2, suggesting that clinopyroxene did not crystallize during the evolution of the melt. These observations are consistent with sample petrography, as the dominant phenocryst assemblage is plagioclase + olivine. MnO and FeO^T (i.e. $FeO + 0{\cdot}8998Fe_2O_3$) do not exhibit obvious trends with respect to SiO_2. Na_2O and K_2O behave as incompatible elements for the range of SiO_2 shown, both increasing with increasing SiO_2 content.

We observe a tight LLD for TiO_2 and P_2O_5 vs SiO_2 below 52 wt %. Above 52 wt % SiO_2, we observe a factor of five range in TiO_2 and P_2O_5 values, falling into three groups (see Fig. 12). One group follows the main LLD. The second group shows decreasing TiO_2 and P_2O_5 (23 of 182 melt inclusions). For this subset, Al_2O_3 and Na_2O show slightly elevated concentrations with respect to the main LLD. These findings are consistent with localized assimilation of a lithology more evolved than the main LLD, possibly Tertiary intrusive rocks (e.g. Lucassen *et al.*, 2004) or evolved ancestral magmas potentially with Ti-magnetite (Reubi *et al.*, 2011). A third group shows higher values of TiO_2 and P_2O_5 (seven of 182 melt inclusions). These samples also have some of the lowest CaO, Al_2O_3, and Na_2O concentrations in the dataset. These data are consistent with formation in a residual, interstitial melt in the crystal mush (e.g. Bouvet de Maisonneuve et al., 2012*a*).

The P_2O_5 values reported here are significantly higher than those reported by Bouvet de Maisonneuve *et al.* (2012*a*) (see Fig. 12). Our melt inclusion data are consistent with observed matrix glass and whole-rock trends. Additionally, the whole-rock values for P_2O_5 reported by Bouvet de Maisonneuve *et al.* (2012*a*) overlap with the whole-rock P_2O_5 values reported in our study. These differences could be attributed to differences in analytical method such as count times, or primary standards.

The chemical compositions of melt inclusions within the black and brown scoria overlap (Fig. 13); therefore, in this study we treat the melt inclusions as a single set. This observation contrasts with those of Métrich *et al.*

Table 6: Representative major element and volatile concentrations in melt inclusions

Sample:	br1-3-3-2012	blk11-MI-5-2011	br1-3-2-2012	BRN6-3-2010*	bk3-2-1-2012	bk1-2-1-2012	blk8-MI-4-2011	blk7-MI-2-2011
MI location:	int	rim	core	core	int	int	int	int
MI size (μm):	90	41	104	18	113	101	40	82
Bubble:	no	no	yes	no	no	no	yes	no
% PEC:	1	4	1	4	0	4	5	3
SiO_2	49·02	49·76	50·21	50·72	50·72	50·74	50·97	51·52
TiO_2	1·08	0·99	0·97	0·95	0·94	0·89	1·08	0·92
Al_2O_3	17·52	16·62	16·71	18·35	18·58	16·96	16·77	17·50
FeOt	11·34	12·29	11·34	9·19	9·45	11·30	11·17	10·05
Fe_2O_3	1·80	1·98	1·80	1·23	1·33	1·69	1·73	1·46
FeO	9·71	10·51	9·73	8·09	8·25	9·78	9·61	8·73
MnO	0·19	0·22	0·14	0·21	0·16	0·17	0·18	0·17
MgO	6·47	6·62	6·46	6·84	6·14	6·48	6·53	6·46
CaO	10·47	9·80	10·35	10·21	10·18	9·99	9·45	9·47
Na_2O	2·97	2·98	2·93	2·78	3·06	2·77	3·02	3·20
K_2O	0·55	0·38	0·50	0·42	0·48	0·38	0·48	0·40
P_2O_5	0·20	0·15	0·19	0·20	0·15	0·15	0·19	0·16
Total*	100·00	100·00	100·00	100·00	100·00	100·00	100·00	100·00
mg#	0·50	0·49	0·50	0·57	0·54	0·51	0·51	0·53
Host Fo	80	79	80	83	82	80	80	81
S (ppm)	n.d.	n.d.	n.d.	n.d.	n.d.	927	1244	1153
Cl (ppm)	n.d.	n.d.	n.d.	n.d.	n.d.	511	549	488
F (ppm)	n.d.	n.d.	n.d.	n.d.	n.d.	305	0	0
H_2O (wt %)	n.d.	0·37	n.d.	n.d.	n.d.	2·01	n.d.	2·05
H_2O error	n.d.	0·14	n.d.	n.d.	n.d.	0·13	n.d.	0·02
CO_2 (ppm)	n.d.	n.d.	n.d.	n.d.	n.d.	138	n.d.	394
CO_2 error	n.d.	n.d.	n.d.	n.d.	n.d.	7	n.d.	25
T (°C)	1218	1180	1212	1179	1206	1173	1158	1185
P (MPa)	n.d.	n.d.	n.d.	n.d.	n.d.	49	n.d.	81
Depth (km)	n.d.	n.d.	n.d.	n.d.	n.d.	2·0	n.d.	3·3

Sample:	blk9-MI-1-2011	BUL4-3-2010*	BUL4-1-2010*	br2-1-1-2012	brn5-MI-1-2011	bk2-8-1-2012	bk4-2-2-2012	bk4-1-1-2012
MI location:	rim	int	int	int	core	core	rim	core
MI size (μm):	34	16	20	30	50	158	65	184
Bubble:	no	yes	yes	no	yes	no	no	no
% PEC:	4	1	0	0	0	1	2	0
SiO_2	51·54	51·55	52·01	52·02	52·20	52·22	52·25	52·65
TiO_2	1·22	1·02	1·11	1·18	1·10	1·10	1·04	1·68
Al_2O_3	15·86	17·54	17·01	17·55	17·59	17·09	16·96	11·99
FeOt	11·53	10·34	10·66	9·92	10·14	9·71	9·94	15·22
Fe_2O_3	1·90	1·57	1·65	2·21	2·26	1·50	1·52	3·14
FeO	9·82	8·93	9·18	7·94	8·11	8·36	8·57	12·39
MnO	0·20	0·25	0·22	0·20	0·19	0·16	0·17	0·23
MgO	6·52	5·74	6·08	5·22	5·25	5·94	5·84	5·99
CaO	8·98	9·59	8·82	9·65	9·51	9·49	9·65	8·29
Na_2O	3·04	3·04	3·01	3·54	3·24	3·34	3·21	2·76
K_2O	0·73	0·55	0·66	0·56	0·59	0·61	0·61	0·55
P_2O_5	0·19	0·21	0·26	0·17	0·19	0·19	0·19	0·33
Total	100·00	100·00	100·00	100·22	100·23	100·00	100·00	100·00
mg#	0·50	0·50	0·50	0·48	0·48	0·52	0·51	0·41
Host Fo	80	79	79	76	77	81	80	68
S (ppm)	400	n.d.	n.d.	512	454	553	577	175
Cl (ppm)	545	n.d.	n.d.	515	597	495	532	454
F (ppm)	0	n.d.	n.d.	300	n.d.	311	324	289
H_2O (wt %)	n.d.	n.d.	2·00	0·68	n.d.	1·70	1·61	2·04
H_2O error	n.d.	n.d.	0·04	0·05	n.d.	0·10	0·10	0·12
CO_2 (ppm)	n.d.	n.d.	n.d.	37	n.d.	44	25	92
CO_2 error	n.d.	n.d.	n.d.	7	n.d.	7	2	5
T (°C)	1171	1193	1219	1197	1192	1196	1176	1190
P (MPa)	n.d.	n.d.	n.d.	13	n.d.	31	26	73
Depth (km)	n.d.	n.d.	n.d.	0·5	n.d.	1·3	1·1	3·0

(continued)

(2010), who proposed, for the Stromboli system, that olivine sourced from Stromboli brown scoria (i.e. 'golden pumice' in their paper) originated from a different magma than their black scoria.

Olivine-hosted melt inclusion trace elements

The multi-element, normal mid-ocean ridge basalt (N-MORB)-normalized trace element plot (Fig. 14) shows the range and average of key elements including

Table 6: Continued

Sample:	bk4-4-1-2012	brn6-MI-1-2011	bk3-4-3-2012	Plate1-2010*	blk9-MI-2-2011	brn4-MI-1-2011	blk5-MI-1-2011	bk2-6-1-2012
MI location:	int	core	int	core	int	int	core	int
MI size (μm):	90	93	105	33	38	106	157	102
Bubble:	no	no	yes	no	yes	no	no	yes
% PEC:	0	0	2	1	3	0	5	0
SiO_2	52·88	52·90	52·93	54·06	54·06	54·08	54·21	54·24
TiO_2	0·73	1·23	0·88	0·82	1·90	1·65	1·43	1·52
Al_2O_3	17·47	14·95	16·87	16·36	14·00	13·01	15·71	13·53
FeOt	9·48	14·13	9·86	10·15	11·04	13·54	10·92	12·23
Fe_2O_3	1·36	2·82	1·54	1·53	1·99	2·71	2·04	2·72
FeO	8·26	11·60	8·48	8·78	9·25	11·11	9·08	9·78
MnO	0·19	0·24	0·18	0·20	0·19	0·21	0·22	0·23
MgO	6·01	4·62	5·79	5·81	5·86	5·48	3·93	5·33
CaO	9·32	7·57	9·01	8·58	8·55	7·46	8·99	8·93
Na_2O	3·25	3·08	3·73	3·11	2·99	2·97	3·36	2·98
K_2O	0·44	0·73	0·46	0·58	0·92	0·98	0·72	0·64
P_2O_5	0·09	0·27	0·14	0·17	0·28	0·35	0·30	0·37
Total	100·00	100·00	100·00	100·00	100·00	100·00	99·99	100·28
mg#	0·53	0·37	0·51	0·51	0·49	0·42	0·39	0·44
Host Fo	81	68	80	80	79	71	72	72
S (ppm)	731	482	995	n.d.	895	104	618	n.d.
Cl (ppm)	352	412	435	n.d.	491	423	512	n.d.
F (ppm)	218	n.d.	257	n.d.	n.d.	n.d.	n.d.	n.d.
H_2O (wt %)	1·90	n.d.	1·96	1·98	n.d.	1·93	n.d.	n.d.
H_2O error	n.d.	n.d.	0·13	0·08	n.d.	0·10	n.d.	n.d.
CO_2 (ppm)	125	n.d.	171	796	n.d.	n.d.	n.d.	n.d.
CO_2 error	7	n.d.	11	155	n.d.	n.d.	n.d.	n.d.
T (°C)	1215	1186	1178	1197	1176	1209	1224	1213
P (MPa)	45	n.d.	55	151	n.d.	n.d.	n.d.	n.d.
Depth (km)	1·8	n.d.	2·2	6·1	n.d.	n.d.	n.d.	n.d.

Sample:	br1-2-1-2012	BLK8-1-2010*	br4-3-3-2012	br1-5-1-2012	brn14-MI-1-2011	brn12-MI-1-2011*	blk1-MI-1-2011	bk3-2-2-2012	BUL1-2010*
MI location:	core	int	rim	core	core	int	core	int	rim
MI size (μm):	131	60	111	42	92	123	236	57	60
Bubble:	no	no	no	no	no	no	no	no	no
% PEC:	0	5	1	0	0	0	0	2	0
SiO_2	54·31	54·38	54·47	54·92	54·93	55·03	55·05	55·15	56·04
TiO_2	1·55	1·35	1·15	1·77	1·70	1·76	1·75	0·65	1·53
Al_2O_3	12·91	16·05	16·65	13·02	13·36	12·85	13·34	16·72	15·13
FeOt	12·98	9·76	9·27	13·49	12·41	13·63	12·61	8·73	10·40
Fe_2O_3	2·50	1·54	1·53	2·85	2·42	2·93	2·56	1·30	1·81
FeO	10·73	8·38	7·90	10·93	10·23	10·99	10·31	7·55	8·78
MnO	0·22	0·16	0·17	0·20	0·26	0·24	0·24	0·17	0·23
MgO	5·77	5·77	5·19	4·63	5·07	4·56	4·79	5·62	4·51
CaO	7·82	8·05	8·12	7·42	7·81	7·18	7·50	8·43	7·60
Na_2O	3·08	3·12	4·04	3·14	3·09	3·11	3·09	3·78	3·06
K_2O	0·84	0·93	0·62	0·84	0·84	1·01	1·06	0·51	0·99
P_2O_5	0·26	0·29	0·16	0·28	0·29	0·34	0·32	0·10	0·32
Total	100·00	100·00	100·00	100·00	100·00	100·00	100·00	100·00	100·00
mg#	0·44	0·51	0·50	0·38	0·42	0·37	0·40	0·53	0·44
Host Fo	73	80	80	69	73	69	72	82	75
S (ppm)	299	n.d.	n.d.	330	258	268	215	n.d.	n.d.
Cl (ppm)	462	n.d.	n.d.	515	412	406	500	n.d.	n.d.
F (ppm)	478	n.d.	n.d.	606	n.d.	n.d.	n.d.	n.d.	n.d.
H_2O (wt %)	1·91	2·17	n.d.	2·12	1·91	2·30	2·00	n.d.	1·69
H_2O error	0·12	0·08	n.d.	0·14	0·04	0·04	0·04	n.d.	0·04
CO_2 (ppm)	259	1226	n.d.	61	584	n.d.	1508	n.d.	750
CO_2 error	21	103	n.d.	9	124	n.d.	96	n.d.	126
T (°C)	1225	1128	1182	1202	1201	1200	1196	1182	1175
P (MPa)	108	205	n.d.	57	174	n.d.	342	n.d.	165
Depth (km)	4·4	8·4	n.d.	2·3	7·1	n.d.	13·9	n.d.	6·7

*These measurements are after post-entrapment correction. Uncorrected data can be found in the Supplementary Data. Melt inclusions labeled int were located between the core and the rim. n.d., not determined.

selected rare earth elements (REE) and large-ion lithophile elements, which are used to provide information about petrogenetic processes. All data collected by LA-ICP-MS are plotted and overlain by the calculated average value; we also included previously reported whole-rock trace element data for Llaima Holocene tephras for comparison (dark gray region; Jacques *et al.*, 2014). Our trace element data show a signature generally

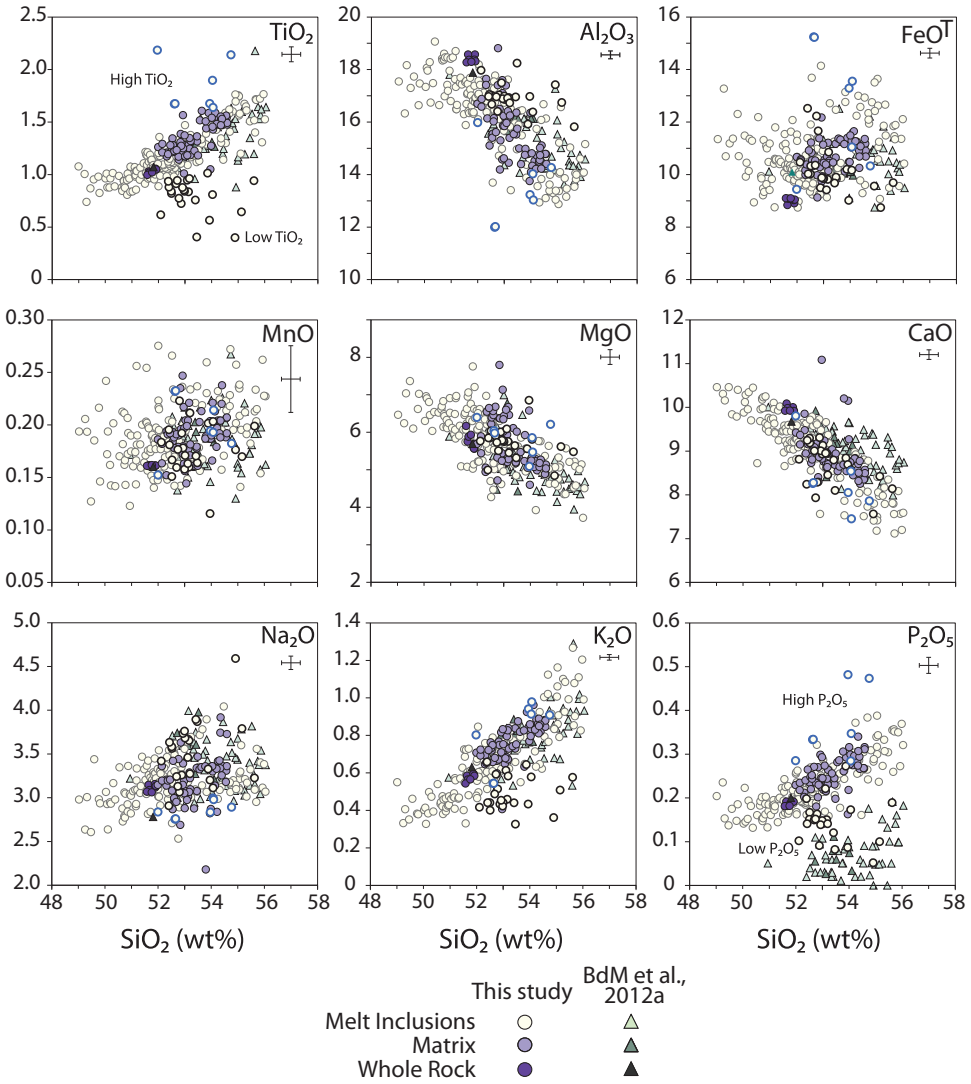

Fig. 12. SiO_2 diagrams showing the range of chemical variation in the melt inclusions, matrix glass, and whole-rock analyses. Samples from Bouvet de Maisonneuve *et al.* (2012*a*) are shown for comparison (triangles; same color scheme for whole-rock, matrix glass, and melt inclusions). The crosses in the upper right corner of each plot represent the average standard deviation of the analyses. CaO, MgO, and Al_2O_3 show negative correlations with SiO_2, consistent with plagioclase and olivine crystallization. K_2O, Na_2O, P_2O_5, and TiO_2 show incompatible behavior. FeO^T and MnO do not show any trends. All values are in wt %. Symbols with dark bold outlines highlight the low-TiO_2 and -P_2O_5 samples, whereas symbols with the blue bold outlines denote samples with high TiO_2 and P_2O_5.

consistent with subduction zone magmas as indicated by enrichments of fluid-mobile elements (e.g. Rb, Ba, K, U, Pb), a negative Nb–Ta anomaly and moderately enriched light REE with respect to heavy REE, as previously reported elsewhere (e.g. Hickey-Vargas *et al.*, 1986; Reubi *et al.*, 2011; Jacques *et al.*, 2014). However, several elemental signatures do exhibit some notable variation from those data in the literature. First, we observe positive Eu anomalies in some of our melt inclusions, and negative Eu anomalies in others. Second, Ba/La in our dataset ranges from 17 to 46, whereas literature values for Llaima range from 23 to 27 (e.g. Reubi *et al.*, 2011; Jacques *et al.*, 2014). Similarly, the range of observed Nb–Ta anomalies is wider than previously reported (see Fig. 14). Conversely, Ce/Pb values in our samples (2–4) overlap well with literature values (2–3) (Reubi *et al.*, 2011; Jacques *et al.*, 2014).

Volatiles in melt inclusions and matrix glass

Volatile contents within the melt inclusions were measured using the methods discussed above; the results are shown in Table 7. H_2O and CO_2 were not measured in the matrix glass because it was not possible to prepare FTIR wafers without crystals that interfered with the path of the IR beam. S and Cl in the matrix glass were measured by EMPA and are in the range of 6–600 ppm and 330–500 ppm, respectively.

FTIR results for H_2O in the melt inclusions range from 0·36 to 2·97 wt %. Similarly, the SIMS analytical results have H_2O contents ranging from 0·57 to 2·37 wt % H_2O. H_2O values correspond to those reported in previous work (Bouvet de Maisonneuve *et al.*, 2012*a*) (Fig. 15). CO_2 values from the FTIR analysis range from 397 to 1973 ppm, contrasting with the lower CO_2 from SIMS analysis (22–274 ppm). We would expect the FTIR

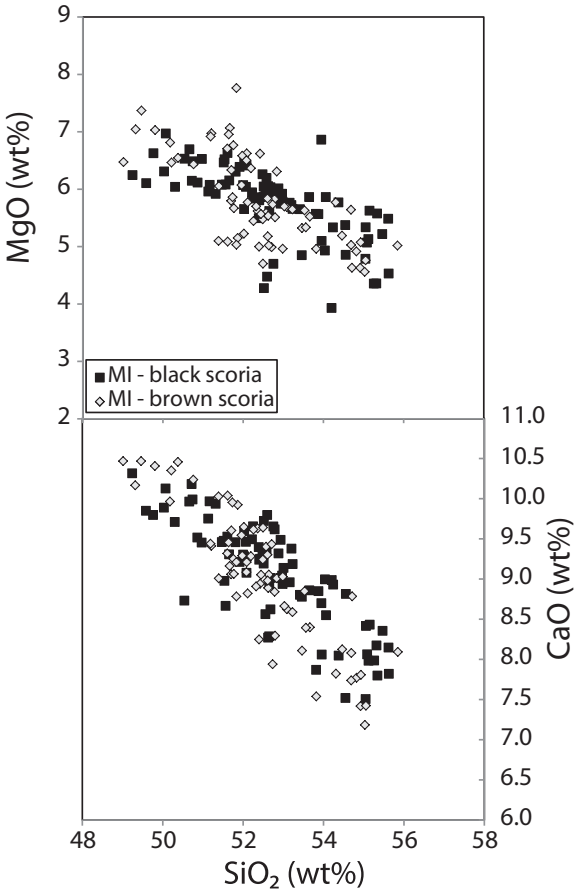

Fig. 13. A comparison of melt inclusions from the black and brown scoria to determine if there are distinct populations. The overlap of these datasets indicates that their respective melt inclusions are indistinguishable in terms of major elements (MgO and CaO).

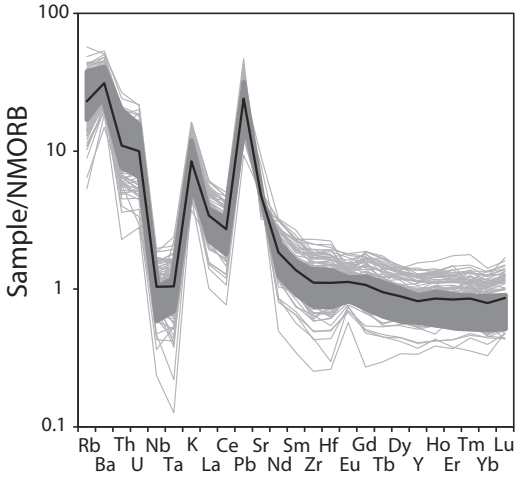

Fig. 14. Multielement N-MORB-normalized trace element plot for all analyzed melt inclusions with the average value shown by the bold black line. The dark gray field represents whole-rock trace element data from Llaima Holocene tephra from Jacques *et al.* (2014). Noteworthy features are the subduction zone signature with enriched large-ion lithophile elements and light rare earth elements with respect to heavy rare earth elements, and the range of Nb–Ta anomalies. Normalization values are from Sun & McDonough (1989).

analysis to record the lower CO_2 contents. However, many of our samples exhibited fringes (e.g. Nichols & Wysoczanski, 2007), the presence of which could have obscured the small CO_3^{2-} doublet that would result from low CO_2 in the melt inclusions. The CO_2 values presented here are the highest measured in recent Llaima samples to date.

Sulfur contents from the EPMA analyses range from 23 to 1534 ppm. SIMS analyses report sulfur abundances from 92 to 1277 ppm. Similarly, chlorine results from EPMA show concentrations from 47 to 1342 ppm, whereas SIMS results show abundances from 236 to 641 ppm.

We were unable to measure volatiles using all techniques on each melt inclusion, thus direct comparisons between the techniques were not possible with this dataset. However, the measured values from SIMS for H_2O, S, and Cl overlap well with those reported from EPMA and FTIR (see Table 7). For S and Cl, the EPMA results show a wider range of values compared with the SIMS results. Similarly, the range of FTIR H_2O concentrations is wider than those obtained via SIMS. CO_2 concentrations measured using SIMS were lower, on average, than those measured using FTIR; however, we were only able to retrieve CO_2 values using FTIR from 12 samples.

Entrapment and magma temperature calculations

Entrapment temperature for each melt inclusion–olivine pair was estimated using olivine–liquid equilibria, which are based dominantly on the Mg partitioning behavior between olivine and the melt and have been calibrated for hydrous melts (Putirka *et al.*, 2007; Putirka, 2008). For this study, we used equation (22) from Putirka (2008), which includes the effect of H_2O on the temperature calculation. H_2O contents measured with FTIR or SIMS were included for the respective melt inclusions. We assumed an anhydrous melt for those melt inclusions without H_2O content data. Using equation (22) from Putirka (2008), the melt inclusion entrapment temperatures ranged from 1094 to 1233°C, with an average of 1175°C. This range of entrapment temperatures strongly suggests that olivine grew in a wide variety of magmatic thermal conditions, and that cooling-induced crystallization was probably an important process.

To further constrain magmatic temperatures in the shallow plumbing system, plagioclase–liquid equilibria, based on the alkali or alkali earth partitioning between the plagioclase and the melt (Putirka, 2008) was also considered. Assuming equilibrium and using the composition of the microphenocryst plagioclase and the anhydrous matrix glass, we estimated the average temperature just prior to eruption at 1146°C (low 1109°C, high 1167°C). We compared these magmatic temperatures with those calculated from the plagioclase hygrometer proposed by Lange *et al.* (2009). Using the matrix glass H_2O values

Table 7: Analytical results (range, average, and standard deviation) for melt inclusion volatiles measured with FTIR, SIMS and EPMA

	H_2O (wt %)	CO_2 (ppm)	S (ppm)	Cl (ppm)	F (ppm)
FTIR	0·36–2·94	394–1973			
(H_2O, $n = 54$; CO_2, $n = 13$)	(1·8 ± 0·61)	(939 ± 473)			
SIMS	0·53–2·37	22–274	92–1277	236–641	155–606
($n = 32$)	(1·76 ± 0·44)	(110 ± 77)	(639 ± 290)	(478 ± 86)	(322 ± 89)
EPMA			23–1534	47–1342	
($n = 47$)			(699 ± 415)	(490 ± 183)	

Standard deviations are 2σ. *n*, number of analyses.

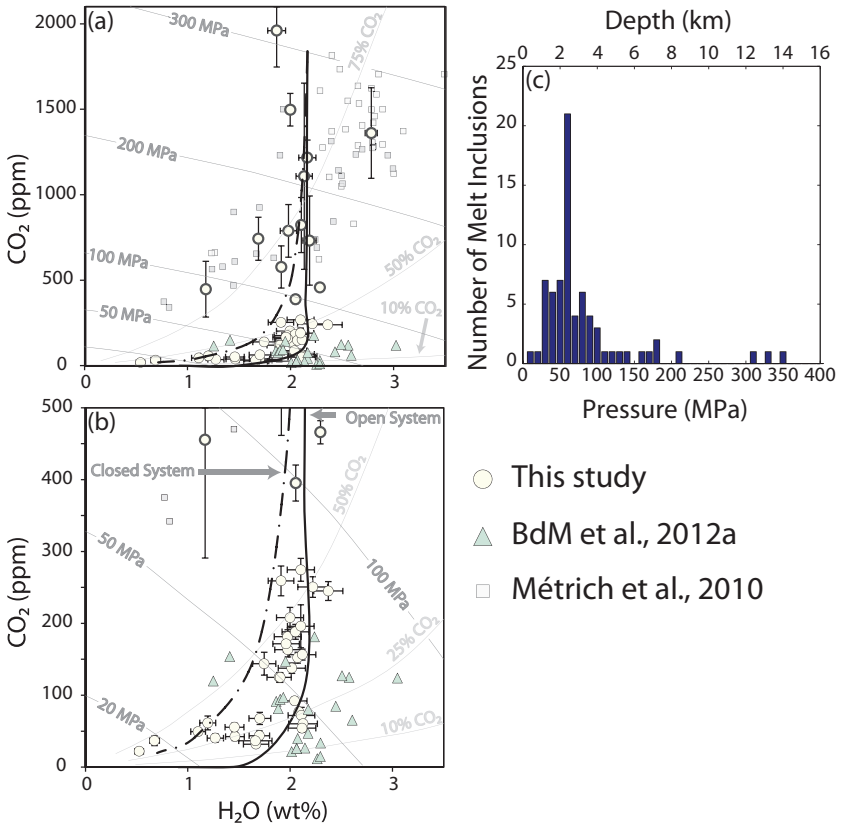

Fig. 15. The model of Papale *et al.* (2006) used to assess degassing style recorded by the melt inclusions. (a) Plots of CO_2 vs H_2O from melt inclusions to show degassing behavior. Bold-outline circles, analyzed by FTIR; regular-outline circles, analyzed by SIMS. The error bars are 2σ. Open (bold continuous black line) and closed (bold dashed black line) system degassing are modelled from 2000 ppm CO_2, 2·15 wt % H_2O. For the closed system, there is also an initial vapor phase of 1%. Dark gray lines are isobars; light gray lines are isopleths showing the per cent CO_2 in the vapor phase. All lines were produced using Papale *et al.* (2006). (b) Close-up version of (a); the vertical scale change should be noted. All symbols are as in Fig. 12. For comparison, melt inclusion volatile contents from paroxysmal eruptions at Stromboli reported by Métrich *et al.* (2010) are also plotted in (a) and (b). (c) Histogram showing the distribution of entrapment pressures for the plumbing system. The peak at 80 MPa should be noted.

(0·88 wt %, rounded to 0·9 wt %; Bouvet de Maisonneuve *et al.*, 2012*a*), the average matrix glass composition (SiO_2 53·36 wt %, TiO_2 1·34 wt %, Al_2O_3 15·56 wt %, FeO^T 10·69 wt %, MgO 5·69 wt %, CaO 8·91 wt %, Na_2O 3·18 wt %, K_2O 0·76 wt %), the average plagioclase composition (An_{69}), and pressure at 50 MPa, we calculated the minimum shallow magmatic temperatures as 1115°C. This is lower than the results from the Putirka model, but within the range of expected uncertainty (±25–30°C) for geothermometers in general (Putirka, 2008). Based on this, we assume the calculated 1146°C temperature to be a maximum magmatic temperature.

Melt inclusion entrapment pressures

The pressure-dependent solubility behavior of CO_2 and H_2O can be used to estimate the entrapment pressures of the single melt inclusions (Dixon *et al.*, 1995; Métrich & Wallace, 2008). That H_2O and CO_2 vary widely in our melt inclusions indicates that melt inclusion formation (and associated olivine crystallization) occurred over a wide range of pressures. Two solubility models have been commonly used to estimate entrapment pressures: VolatileCalc (Newman & Lowenstern, 2002) and the Papale *et al.* (2006) model. Moore (2008) established that the Papale model was the best choice for calc-alkaline

magmas because VolatileCalc neglects the effect of Ca on CO_2 solubility. It should be noted that we did not correct for the possible CO_2 migration into vapor bubbles in the melt inclusions and, therefore, consider these values as minimum entrapment pressures. The entrapment pressures for our suite of melt inclusions range from 8 to 342 MPa, based on the Papale model (Fig. 15). Assuming a crustal density of 2500 kg m^{-3}, depths range between ~340 m and 13·9 km. We observe a strong peak between 50 and 100 MPa (1–4 km), suggesting a crystal-rich region (i.e. a crystal mush). These data increase the depth of the crystallizing portion of the plumbing system as reported by Bouvet de Maisonneuve *et al.* (2012*a*) by a factor of three.

DISCUSSION

System-wide processes

Magmatic evolution

The majority of our dataset shows evidence for a connected magmatic system that fractionates olivine + plagioclase. The most primitive melt inclusions follow the main LLD (see Fig. 12). More compositional variability is observed in melt inclusions with >52 wt % SiO_2. Low-TiO_2 melt inclusion compositions are most consistent with assimilation of more evolved lithologies, probably with SiO_2 values between 56 and 58 wt % and very low TiO_2 and P_2O_5. These could represent the basement Tertiary intrusive rocks (e.g. Lucassen *et al.*, 2004) or evolved ancestral magmas (Reubi *et al.*, 2011). Positive Eu anomaly values (1·10 ± 0·24) are indicative of plagioclase dissolution, which supports assimilation. This assimilation occurred within the inferred crystal mush zone as indicated by entrapment pressures ranging from 50 to 150 MPa. Our interpretation is consistent with previous work suggesting that limited assimilation occurs potentially as a late-stage shallow process (e.g. Reubi *et al.*, 2011).

The high-TiO_2 melt inclusions have elevated P_2O_5 and K_2O, and low values of Al_2O_3 and CaO. Eu anomaly values average 0·77 ± 0·05, indicative of plagioclase fractionation. These data are consistent with melt inclusion formation in melts that fractionated a higher modal abundance of plagioclase than the main LLD inclusions. We propose that these melt inclusions formed from interstitial melts in crystal-rich regions in the plumbing system (e.g. Bouvet de Maisonneuve *et al.*, 2012*a*). Only two melt inclusions from the high-TiO_2 group have pressure estimates and these are 73 and 309 MPa, respectively. The latter entrapment pressure possibly suggests that crystal-rich zones with evolved interstitial melts may be present in the deep system, as well as the crystal mush. Although we cannot quantitatively link the number of melt inclusions to magma volumes, the large number of melt inclusions analyzed ($n = 182$) suggests that melt inclusions from the high-TiO_2 ($n = 7$, 3·8% of the sample suite) and low-TiO_2 ($n = 23$, 13% of the sample suite) groups both represent volumetrically minor amounts of magma compared with the main LLD. Our dataset contrasts with previously reported interpretations that suggest that melt inclusions dominantly formed in isolated melts with different evolution histories (Bouvet de Maisonneuve *et al.*, 2012*a*).

Degassing and crystallization

The melt inclusions display a wide range of CO_2 contents, from below detection to nearly 2000 ppm, but tightly cluster near 2 wt % water down to CO_2 contents of ~100 ppm. The population of inclusions with CO_2 below 100 ppm and with 2 wt % water argues for open-system degassing (Fig. 15). In this work, we understand open-system degassing as the process in which volatiles exsolve, decouple from the parent magma and then escape through bubble ascent (i.e. fractional degassing) (Dixon & Stolper, 1995; Cashman, 2004). Our findings contrast with previous studies that suggest that explosive eruptions in mafic systems result from rapid magmatic ascent under closed-system degassing conditions (e.g. Coltelli *et al.*, 2005; Métrich & Wallace, 2008). For example, paroxysmal eruptions (i.e. violent Strombolian) at Stromboli show distinctly different degassing trends (Fig. 15a), which have been interpreted to record closed-system degassing and magma+volatile ascent (Métrich *et al.*, 2010). In closed-system degassing, volatiles exsolve to form a vapor phase, and then remain with the parent melt (i.e. equilibrium degassing). When magma ascent is rapid, the vapor phase increases in volume fraction, and as it is coupled to the magma it leads to explosive fragmentation. Although passive degassing processes at the summit have been linked elsewhere to open- and/or closed-system degassing processes in deeper plumbing systems (e.g. Burton *et al.*, 2007), the melt inclusion evidence for open-system degassing at Llaima indicates that volatiles, even at depth, are decoupled from the magma, and allowed to ascend. Therefore, to produce the 2008 violent Strombolian eruption, a mechanism must be invoked that can explain the observed transition from passive degassing to explosive activity, but is independent of the established deeply rooted passive degassing system.

Water loss through degassing promotes crystallization (e.g. Crabtree & Lange, 2011; Applegarth *et al.*, 2013). Although crystallization does occur during syn-eruptive cooling and degassing, melt inclusion entrapment in olivine is not likely to occur syn-eruption. We explored the relationship between degassing and crystallization by comparing the respective proxy ratios (e.g. Blake *et al.*, 2010; Johnson *et al.*, 2010). Figure 16 displays the volatile/K_2O ratios for H_2O, S, Cl, and CO_2 versus MgO/K_2O. If crystallization occurred without degassing, the data would follow a horizontal trend. If degassing was dominant, the data would follow a vertical trend. Our results show strong correlations between MgO/K_2O and H_2O/K_2O, Cl/K_2O, and S/K_2O, indicating that degassing and crystallization are coupled

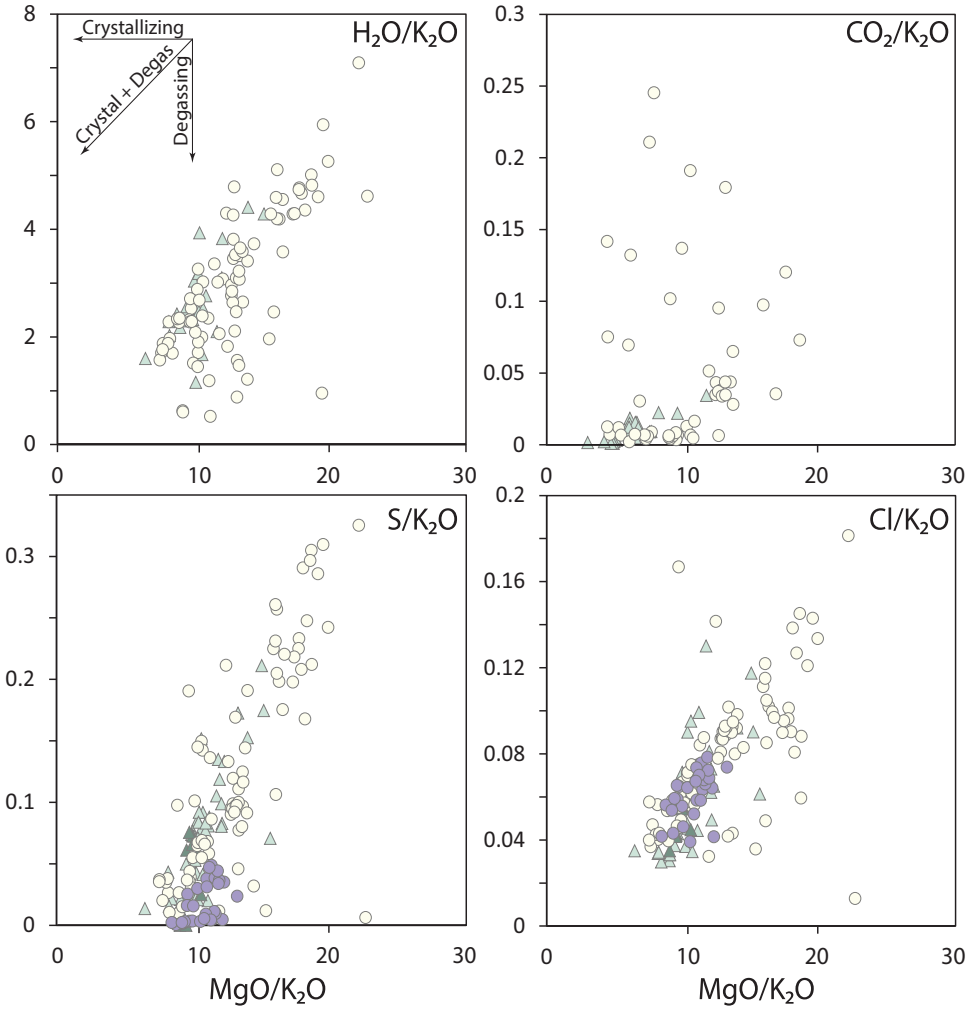

Fig. 16. Volatile ratios to K_2O to show the relationship between degassing and crystallization. H_2O, S, and Cl show good correlations with K_2O, indicating that degassing and crystallization are coupled. CO_2 shows more scatter, but at lower values (i.e. inferred shallower levels) degassing and crystallization are coupled. Matrix glass values for S and Cl provide information about degassing during the eruption. Both Cl and S in the matrix glass decrease, indicating syn-eruption degassing. Very low S values in the matrix glass suggest almost complete degassing, whereas Cl did not completely degas. Symbols as in Fig. 12.

processes. CO_2/K_2O is correlated with MgO/K_2O at lower CO_2 values (i.e. lower pressures), but does not correlate at higher CO_2 values. Indeed, the majority of the sample suite falls on the coupled crystallization and degassing trend, including samples with high volatile contents (e.g. high volatile/K_2O ratios). Similarly, scoria matrix glass values fall on the trend with some of the lowest S/K_2O and Cl/K_2O values in the dataset. This indicates that the matrix glass was almost completely degassed as a result of crystallization. Some melt inclusions have similarly low S/K_2O values, suggesting that the melt inclusions trapped largely degassed magma. These inferences suggest that crystallization and, importantly, degassing were coupled in the deep plumbing system (at least to 14 km depth), as well as in the shallow system. These data combined with the wide range of olivine entrapment temperatures suggest that cooling-induced and degassing-induced crystallization processes may be equally important.

Shallow system processes—passive degassing

Textural maturation and the formation of black and brown scoria

The brown scoria exhibits textures indicative of rapid vesicle nucleation at relatively high undercooling (i.e. higher intercept on the CSD plot and high vesicle number density). The inferred initial stages of vesicle ripening in the brown scoria probably occurred during ascent in the conduit just before quenching. Similar interpretations and short timescales were presented for vesicle ripening in reticulite from Hawaii (e.g. Mangan & Cashman, 1996). Conversely, textural data from the black scoria suggest a rapid nucleation event but also more prolonged crystal growth, with vesicle textures suggesting steady-state nucleation with possibly some coalescence. These data are indicative of longer residence times before eruption. Together, the observed textures are indicative of a continuum of textural maturation from the brown to black scoria that we propose

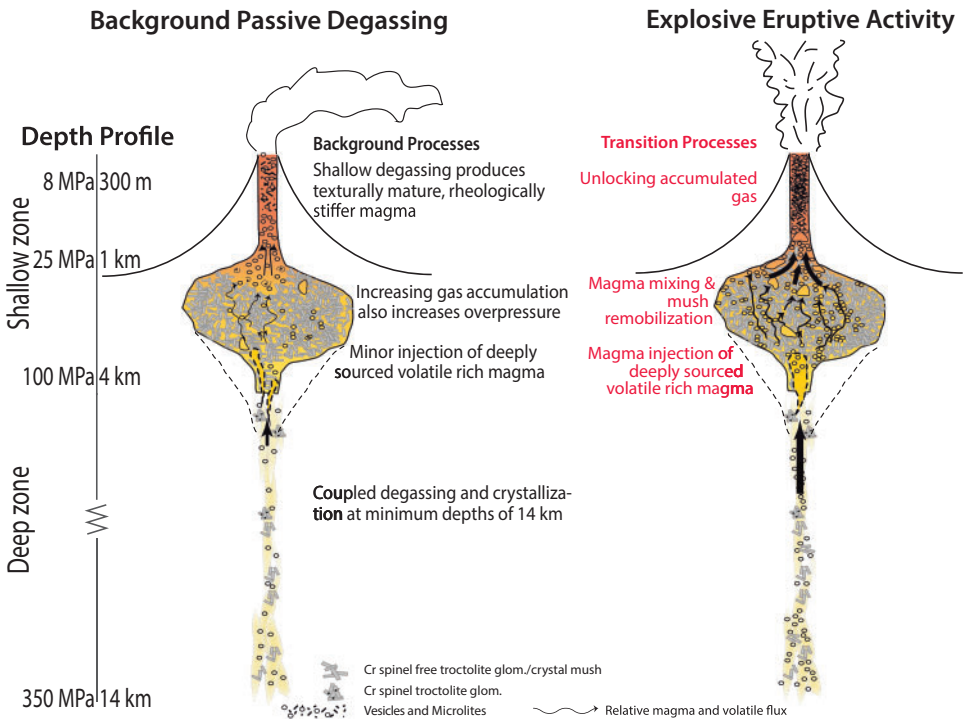

Fig. 17. Schematic illustration of the plumbing system of Llaima and the key magmatic processes for the background passive degassing and transitions to the explosive eruption, respectively. Background passive degassing is characterized by continuous degassing from the summit, which results in the crystallization and rheological stiffening of the conduit magma. Minor volumes of magma are periodically injected into the crystal mush, which degasses and maintains the summit degassing. The deep plumbing system also experiences crystallization and degassing. Gas transport through the system is regulated mostly by the presence of the crystal mush, where vesicles become trapped within the interstitial spaces between crystals. Additional gas holdup may occur beneath the rheologically stiffer conduit magma. Gas may develop into larger bubbles, or more probably, foamy regions in the upper part of the crystal mush (the larger vesicles in the figure). The transition to the 2008 eruption at Llaima occurred after an injection event that remobilized the crystal mush and, importantly, unlocked the accumulated gas, which ascended rapidly to produce the observed explosive behavior at the summit.

results from background passive degassing. The presence of normally zoned microphenocryst plagioclase predominantly in the black scoria supports this, as it suggests growth-dominated conditions associated with lower, possibly steady-state, rates of degassing (Cashman, 2004; Castro *et al.*, 2005). In summary, the textural features of the black scoria reflect passive degassing conditions in the conduit and probably represent magma slowly circulating within the shallow plumbing system.

Texturally bimodal scoria was first observed and described at Stromboli (Francalanci *et al.*, 2004) and has since been observed in other systems (e.g. Croscat complex cone system; Cimarelli *et al.*, 2010). The formation of texturally bimodal scoria in explosive systems has been attributed to two processes, depending on whether they are geochemically distinct or not. Where scoria originated from geochemically similar magmas, sourced from similar locations within the shallow plumbing system, textures are interpreted to record end-members on a textural maturity continuum (Lautze & Houghton, 2007; Cimarelli *et al.*, 2010; Erlund *et al.*, 2010). In these cases, differences between scoria types are a function of the physical processes experienced. Alternatively, where distinctions can be made in the geochemistry, such as melt inclusion chemistry, the source magmas for the different scoria are chemically distinct and originate from different locations in the system (Métrich *et al.*, 2001, 2010). At Llaima, the geochemical similarity of the scoria whole-rock compositions (Fig. 12) and the fact that melt inclusions from the different scoria overlap (Fig. 13) indicate that differences are textural alone, and probably formed as a result of differing degassing histories, rather than from geochemically different magmas (at least with respect to major element chemistry).

Plumbing system conceptual model

Summarizing the scoria textures, olivine-hosted melt inclusions, as well as findings from previous work (e.g. Bouvet de Maisonneuve *et al.*, 2012*a*, 2012*b*; Ruth & Calder, 2014) we present here a conceptual model of the plumbing system at Llaima from the vent to ~14 km depth (Fig. 17). We infer two magma accumulation regions based on the clustering of melt inclusion entrapment pressures (histogram in Fig. 15). The main magmatic region is the shallowest, extending from the conduit (300 m) to ~4 km depth. Magma that produced the black 'resident' scoria is probably sourced from this region. Most melt inclusions formed (or re-equilibrated)

Table 8: Inputs and viscosity modeling results based on different crystallinity in the scoria

Model inputs:	SiO_2	TiO_2	Al_2O_3	Fe_2O_3	FeO	MnO	MgO	CaO	Na_2O	K_2O	P_2O_5	H_2O	T(°C)
	51·35	1·02	18·25	2·76	8·94	0·16	5·75	9·89	3·09	0·57	0·19	1·0	1150
Viscosity (Pa s):	8 MPa		15 MPa		30 MPa								
	Shaw	B&W	Shaw	B&W	Shaw	B&W							
Black scoria, 50% crystallinity	$5{\cdot}64 \times 10^4$	$2{\cdot}80 \times 10^4$	$2{\cdot}29 \times 10^4$	$2{\cdot}35 \times 10^4$	$2{\cdot}29 \times 10^4$	$2{\cdot}35 \times 10^4$							
Brown scoria, 10% crystallinity	$1{\cdot}33 \times 10^2$	$1{\cdot}59 \times 10^2$	$4{\cdot}45 \times 10^1$	$5{\cdot}40 \times 10^1$	$4{\cdot}45 \times 10^1$	$5{\cdot}40 \times 10^1$							

Model inputs include the average whole-rock chemistry with all major elements in wt %, assumed water content of 1 wt %, and the temperature from the plagioclase melt thermometer. The reported values are for both the Shaw (1972) model and the Bottinga & Weill (1972) model.

at pressures from 50 to 100 MPa. This strongly supports the crystal mush zone proposed in previous work (e.g. Bouvet de Maisonneuve *et al.*, 2012*a*, 2012*b*). Crystallization of olivine and plagioclase occurred throughout the plumbing system as indicated by the main LLD. Minor amounts of localized assimilation of evolved lithologies occurred in the crystal mush zone (e.g. low-TiO_2 melt inclusions, 50–150 MPa entrapment pressures). High-TiO_2 and -P_2O_5 melt inclusions with similar crystal mush pressures also indicate entrapment of interstitial melts. Reverse zoning in olivine crystals suggests this as the main region of magma mixing (Bouvet de Maisonneuve *et al.*, 2012*b*; Ruth, 2014). This magma mixing probably produced the multiply zoned plagioclase and the sieve textured plagioclase phenocrysts, textures that form under dynamic conditions, especially with respect to magmatic H_2O and temperature (Landi *et al.*, 2004; Streck, 2008; Crabtree & Lange, 2011; Bouvet de Maisonneuve *et al.*, 2012*b*). Because plagioclase crystals within the Cr-spinel-free troctolite glomerocrysts have similar sieve textures, we infer that they are also sourced from the crystal mush zone.

Olivine-hosted melt inclusions show that the deeper plumbing system extends from 4 to 14 km depth. Although we do not have many samples from the deep system, we infer information about the processes occurring within this region from melt inclusion chemistry and the Cr-spinel troctolite glomerocrysts. Degassing occurs at up to 14 km depth, and is coupled with crystallization. Extensive crystallization is suggested by the one melt inclusion with high TiO_2 and P_2O_5 with a high entrapment pressure, which may have formed in the interstitial melts within this region. Moreover, the presence of Cr-spinel in some troctolite glomerocrysts is consistent with deeper origins from magmas that have experienced limited fractionation (e.g. Streck *et al.*, 2002); these are most likely to be found at greater depths than the main crystal mush zone. This potentially suggests a crystal-rich zone in the deeper system (e.g. Annen *et al.*, 2006). Similar crystal-rich zones have been proposed for the deeper system beneath Mt Etna (e.g. Laiolo & Cigolini, 2006).

Changes in magmatic physical properties owing to passive and syn-eruption degassing

Magma viscosity is affected by crystal abundance and morphology, which can be altered as a result of degassing processes. Analog experiments show that increasing microlite abundance with respect to phenocryst abundance can potentially increase effective viscosity by up to three orders of magnitude (Cimarelli *et al.*, 2011). The effective viscosity may increase further as a result of syn-eruption (or passive) degassing and crystallization. Heating experiments on volatile-poor porphyritic basalts reveal that rapid, significant degassing and crystallization (up to 35%) can occur in degassed conduit melts, resulting in additional dendritic to spherulitic crystal nucleation on existing crystals (i.e. overgrowths) (Applegarth *et al.*, 2013, figs 12 and 13). We estimated the viscosity indirectly using the MAGMA software package (version 2.50.0133 http://www.lanl.gov/orgs/ees/geodynamics/Wohletz/KWare/Index.htm), the average whole-rock composition, and the average total crystallinity of the brown and black scoria (for results see Table 8). The majority of the crystallinity in both cases is in the form of microlites, as the phenocryst content for both scoria types is less than 10%. The brown scoria magma has a vesicle-free effective viscosity ranging from $5{\cdot}4 \times 10^1$ to $1{\cdot}33 \times 10^2$ Pa s. The black scoria magma has a vesicle-free effective viscosity that is generally two to three orders of magnitude higher ($2{\cdot}29 \times 10^4$ to $5{\cdot}64 \times 10^4$ Pa s). Our first-order approximation of the viscosity differences is consistent with findings reported by Cimarelli *et al.* (2011). Additionally, in the black and brown scoria we observe dendritic overgrowth textures similar to those reported by Applegarth *et al.* (2013), especially around boundaries between textural domains (Fig. 5d), and near vesicles and fractures (see Supplementary Data Fig. S3). The proximity to vesicles, in particular, suggests formation resulting from late-stage degassing. Based on the experimental results from the literature and our textural data, we propose that significant viscosity changes resulted from both passive degassing prior to, and syn-eruptive degassing during, the 2008 eruption at Llaima.

Transitions in eruptive style at Llaima

Maintenance of an open conduit commonly associated with passive degassing requires that heat and magma be continually replenished (Kazahaya *et al.*, 1994; Stevenson & Blake, 1998). Heat and magma supply to the upper plumbing system can occur through density-driven convective mixing between the degassed and

cooler shallow magmas and relatively volatile-rich and hotter deeper magmas (Kazahaya *et al.*, 1994; Allard, 1997; Stevenson & Blake, 1998; Beckett *et al.*, 2014). An additional mechanism for inducing axial mixing that is likely to be important is that the ascending gas flux in a conduit will itself drive a return flow of magma (Pansino, 2012).

We propose that the background activity at Llaima is maintained through periodic small-batch mafic injections, as indicated by crystal zoning, into the base of a crystal mush (1–4 km depth) (Fig. 17). Resultant hybrid magmas with initially moderate H_2O contents (~2 wt %) are mobilized and entrained into the axial mixing processes. The ascent and mixing results in degassing and crystallization, and we speculate that this magma would ultimately result in the black scoria type products with the observed mature crystal and vesicle textures.

For the 2008 eruptive episode, magma injection and mush remobilization, as indicated by reversely zoned olivine (e.g. Bouvet de Maisonneuve *et al.*, 2012*a*, 2012*b*; Ruth, 2014), have been proposed as a triggering mechanism (Bouvet de Maisonneuve *et al.*, 2012*a*). However, the lack of significant ground deformation prior to the eruption suggests that any magma injection into the system must have been volumetrically minor (Remy *et al.*, 2015; Delgado *et al.*, in preparation). Furthermore, violent Strombolian eruptions are highly pulsatory in nature and require high mass and gas fluxes to drive them (Pioli *et al.*, 2009). Therefore, any robust discussion of the triggers of such an eruption must account for substantial gas accumulation and its rapid ascent. Three mechanisms of potential gas accumulation are discussed below.

1. Crystal mush zones may facilitate gas accumulation. Analog experiments suggest that small vesicles can become trapped within particle-rich suspensions (i.e. gas holdup), which may regulate gas flux through the plumbing system (Belien *et al.*, 2010; Tran *et al.*, 2015). Populations of small vesicles can be added to the crystal mush through volatile saturation and subsequent nucleation. A crystal mush zone at Llaima is inferred at depths between 1 and 4 km, based on the melt inclusion entrapment pressures. With the average whole-rock composition, and 2 wt % H_2O, saturation pressures [calculated using Papale *et al.* (2006)] are between 70 and 80 MPa (~3 km depth); thus it would be reasonable to expect vesicle nucleation within this region. Cr-spinel-free troctolite glomerocrysts contain matrix glass with vesicles, lending further support to this hypothesis. These vesicles may have formed during syn-eruption ascent, but their convoluted morphologies suggest some maturity. Furthermore, ascending CO_2-rich vesicles from depth may also be partially trapped in the crystal mush (Thomas *et al.*, 1993; Costa *et al.*, 2006). The passive degassing behavior at the summit and the open-system degassing signature of the melt inclusions indicate that gas bubbles within the system are mobile. Some mobility may occur owing to crystal settling within the mush (e.g. Boudreau, 2016), with some bubble ascent feeding the passive degassing. However, significant bubble ascent might be inhibited by the surrounding crystals. We propose that gas accumulates within the mush until a critical gas volume is reached. Once the bubbles are released from the crystal mush via remobilization (i.e. unlocked) the accumulated gas would ascend rapidly to generate explosive activity (e.g. Vergniolle & Jaupart, 1990; Parfitt & Wilson, 1995).
2. Extensive passive degassing could result in increased viscosity for the magma residing within the upper conduit. Over time, this magma would stagnate and potentially form a rheologically stiffer (but still permeable) cap, above which magma circulation does not take place. Experimental work suggests that rheological barriers lead to elevated gas overpressures, ultimately increasing the intensity of Strombolian eruptions (Del Bello *et al.*, 2015). Although we do not have direct evidence for such a rheological barrier, the black scoria and plate tephra from the 2008 eruption have textures consistent with prolonged residence and slightly higher viscosities (relative to crystal-free magmas of the same composition), as implied by their higher crystallinities (Table 8). Moreover, with increased viscosity, vesicle coalescence and growth could be retarded (Cashman, 2004; Tran *et al.*, 2015), further augmenting gas accumulation beneath the barrier.
3. Complex plumbing system geometry involving sills could provide additional traps for gas accumulation. Experimental results indicate that sills in passively degassing systems may serve as effective traps by segregating gas via buoyant exchange flow between the sill and conduit (Menand & Phillips, 2007). The plumbing system geometry of Llaima is not well constrained. Regional tectonics and the alignment of vents may indicate that the plumbing system follows a NE–SW orientation (Cembrano & Lara, 2008; Schonwalder-Angel, 2015). However, there is limited discussion of sills and/or other subhorizontal bodies. Recent studies using InSAR have inferred the presence and inflation (6–15 cm) of a sill to the west of the summit at ~5 km depth prior to a subsequent explosive phase on 3 April 2009 (Delgado *et al.*, in preparation); there is assumed post-eruptive subsidence after this event. Although inflation was not observed before the 2008 eruption, the findings of Delgado *et al.* (in preparation) do suggest that a potential short-lived trap for magma and gas accumulation could have occurred.

We propose the following scenario to explain the transition to the violent Strombolian eruption at Llaima on 1 January 2008 (Fig. 17). The eruption occurred in a system that was already passively degassing, which was probably sustained by repeated minor magma injection

events. Upon injection these magma batches degassed volatiles that partially filtered through the crystal mush. Simultaneously, some of these volatiles, as well as volatiles ascending from depth, accumulated in the mush and under the stiffened conduit magma until a critical gas volume was reached. Disruption and remobilization of the mush by injecting magmas unlocked the accumulated gas phase, which ascended rapidly to generate the explosive activity at the vent. Clearing the upper portions of the shallow magma reservoir allowed rapid, and probably chaotic, ascent of the deeper, relatively volatile-rich, magma from depths up to 14 km. Partial mixing between the influx, crystal mush and the resident magma produced the glomerocrysts and the crystal-rich domains represented by the clots of black scoria in the brown scoria (Fig. 5b). Thus magma injection and gas accumulation processes equally contributed to eruption triggering.

Explosive eruptions in mafic systems

Explosive mafic eruptions are commonly associated with closed-system degassing and ascent of magmas from depth (e.g. Roggensack *et al.*, 1997; Métrich *et al.*, 2010). Bouvet de Maisonneuve *et al.* (2012*a*, 2012*b*) suggested that the dominant cause of the 2008 explosive eruption of Llaima was an injection-related, heat-induced rheological change in a crystal mush. We agree with Bouvet de Maisonneuve *et al.* (2012*a*, 2012*b*) that magma injection is an important contribution in triggering the eruption. However, the injection and remobilization model alone does not fully explain the transition from a passive summit degassing system that continuously leaks gas to an explosive eruption characterized by pulsatory behavior that must be related to gas accumulation (Pioli *et al.*, 2009). Previous studies of mafic volcanoes elsewhere highlight the importance of accumulated gas in producing explosive and pulsatory behavior (e.g. Pioli *et al.*, 2008; Andronico *et al.*, 2009; Belien, 2011; Preece *et al.*, 2016). Gas accumulation within crystal mushes has been invoked to explain eruptive behavior in intermediate to silicic systems (Sisson & Bacon, 1999; Pistone *et al.*, 2015; Edmonds *et al.*, 2016). We would have more insight into this process if comparable studies of gas accumulation within mafic systems were available. Additionally, magma reservoirs with accumulated gas are more compressible, and thus able to accommodate more influx with limited ground deformation (Voight *et al.*, 2010); this could explain the lack of observed ground deformation prior to the 2008 activity. Therefore, we posit that gas accumulation within the crystal mush, as well as other traps within the upper plumbing system, and its subsequent sudden disruption and ascent is an equally important contribution to eruption triggering. The proposed mechanism provides an alternative means for mafic systems to generate explosive eruptions that does not rely on rapid ascent of magmas under closed-system degassing conditions. This is especially pertinent for understanding major explosive eruptions in mafic systems such as Llaima that exhibit a dominantly, open-system degassing signature.

CONCLUSIONS

We conducted an extensive geochemical and textural study of the products from the 2008 eruption of Llaima. Our aim was to establish how the processes associated with the explosive eruption initiate and occur, specifically in the context of the established background passive degassing of the system. Here we present the three main conclusions from this work.

1. Texturally bimodal scoria were observed and analyzed. Crystal and vesicle size distributions reveal quantitative textural differences between the 'brown' and 'black' scoria from the 2008 eruption of Llaima Volcano. The black scoria samples generally have higher crystal number densities and larger vesicles, whereas the brown scoria have lower crystal number densities and smaller vesicles. Overall, this suggests increasing textural maturation from the brown to the black scoria. Black scoria probably formed from magma that had experienced prolonged passive degassing and crystallization in the shallow conduit, whereas the brown scoria is characterized by features resulting from rapid syn-eruptive ascent, degassing and crystallization.
2. Our dataset provides the first evidence for an extended deep mafic plumbing system based on olivine-hosted melt inclusions that sampled magmas that range from 49 to 56 wt % SiO_2 at pressures from 8 to 342 MPa (300 m to ~14 km). The majority of samples formed at pressures between 50 and 100 MPa, consistent with a shallow crystal mush. Major elements record a main LLD consistent with plagioclase and olivine fractionation in a well-connected system. Two smaller groups of melt inclusions show higher and lower TiO_2 and P_2O_5 with respect to the main LLD. Low-TiO_2 and -P_2O_5 samples suggest localized assimilation of more evolved lithologies. The high-TiO_2 samples may have formed in isolated pockets of evolved melt; they form at both high and low pressures suggestive of extensive crystallization throughout the system. H_2O and CO_2 in the majority of the melt inclusions show evidence for open-system degassing, which is coupled with crystallization throughout the system.
3. Based on the combined textural and geochemical data, we propose that the main magmatic locus is a crystal mush, located between 1 and 4 km depth. Small volumes of magma from the deeper system are periodically injected, quasi steady state, into the shallow system. This contributes to maintaining passive degassing at the summit. We propose that concurrent with the passive degassing, gradual gas accumulation in the crystal mush and below the rheologically stiffer upper conduit magma occurred

over time, such that a critical gas volume in the system was reached and the system overpressure was surpassed by magma injection prior to the 2008 eruption. Magma remobilization unlocked the accumulated gas, which was able to ascend rapidly and generate the observed explosive and pulsatory activity at the summit. Our proposed scenario provides an alternative model to those that posit that explosive mafic volcanism results from rapid ascent of magma under closed-system degassing conditions. This mechanism provides a means for systems with dominantly open-system degassing behavior to make a transition from passive degassing to violent explosive eruptions.

FUNDING

This work was funded by the Geological Society of America (Graduate Student Research Grant to D.C.S.R.), the Smithsonian Institution (Graduate Fellowship to D.C.S.R.), the Society of Economic Geology (Hugh McKinstry Student Research Grant 11-85 to D.C.S.R.), and the National Science Foundation (EAR-0828070 to E.S.C. while at the University at Buffalo). The ion microprobe facility at the Northeast National Ion Microprobe Facility at Woods Hole Oceanographic Institution was partially subsidized by the Instrumentation and Facilities Program, Division of Earth Sciences, National Science Foundation.

SUPPLEMENTARY DATA

Supplementary data for this paper are available at *Journal of Petrology* online.

ACKNOWLEDGEMENTS

We thank D. Schonwalder-Angel, E. Breard, R. Leach, P. Whelley, and A. Brownell for help in the field, and C. Bouvet de Maisonneuve, O. Bachmann, M. Brounce, J. Ball, A. Graettinger, and G. Valentine for helpful discussions. T. Gooding helped immensely with sample preparation. T. Rose and S. Lynton helped with data collection at the Smithsonian. M. Lytle helped with the LA-ICP-MS analyses. J. Herrin aided with the spinel analyses at Nanyang Technological University. N. Shimizu and B. Monteleone aided with the SIMS measurements. M. Ruth wrote the MATLAB script to correct for fringes in the FTIR spectra. We thank D. Geist, T. Hansteen, and two anonymous reviewers for constructive and helpful comments. We finally thank Marjorie Wilson for her editorial help and patience during the revision process.

REFERENCES

Abbey, S. (1983). Studies in 'Standard Samples' of Silicate Rocks and Minerals 1969–1982. *Can adian Geological Survey Paper* **83-15**, p. 114.

Allard, P. (1997). Endogenous magma degassing and storage at Mount Etna. *Geophysical Research Letters* **24**, 2219–2222.

Andronico, D., Cristaldi, A., Del Carlo, P. & Taddeucci, J. (2009). Shifting styles of basaltic explosive activity during the 2002–2003 eruption of Mt. Etna, Italy. *Journal of Volcanology and Geothermal Research* **180**, 110–122.

Annen, C., Blundy, J. D. & Sparks, R. S. J. (2006). The genesis of intermediate and silicic magmas in deep crustal hot zones. *Journal of Petrology* **47**, 505–539.

Applegarth, L. J., Tuffen, H., James, M. R. & Pinkerton, H. (2013). Degassing-driven crystallization in basalts. *Earth-Science Reviews* **116**, 1–16.

Aster, E. M., Wallace, P. J., Moore, L. R., Watkins, J., Gazel, E. & Bodnar, R. J. (2016). Reconstructing CO_2 concentrations in basaltic melt inclusions using Raman analysis of vapor bubbles. *Journal of Volcanology and Geothermal Research* **323**, 148–162.

Barberi, F., Rosi, M. & Sodi, A. (1993). Volcanic hazard assessment at Stromboli based on review of historical data. *Acta Vulcanologica* **3**, 173–187.

Beckett, F. M., Burton, M., Mader, H. M., Phillips, J. C., Polacci, M., Rust, A. C. & Witham, F. (2014). Conduit convection driving persistent degassing at basaltic volcanoes. *Journal of Volcanology and Geothermal Research* **283**, 19–35.

Belien, I. L. M. B. (2011). Gas migration through crystal-rich mafic volcanic systems and applications to Stromboli Volcano, Aeolian Islands, Italy. PhD dissertation, University of Oregon, Eugene, 188 pp.

Belien, I. B., Cashman, K. V. & Rempel, A. W. (2010). Gas accumulation in particle-rich suspensions and implications for bubble populations in crystal-rich magma. *Earth and Plan etary Science Letters* **297**, 133–140.

Bertagnini, A., Métrich, N., Landi, P. & Rosi, M. (2003). Stromboli volcano (Aeolian Archipelago, Italy): An open window on the deep-feeding system of a steady state basaltic volcano. *Journal of Geophysical Research* **108**(**B7**), doi:10.1029/2002JB002146.

Blake, S., Self, S., Sharma, K. & Sephton, S. (2010). Sulfur release from the Columbia River Basalts and other flood lava eruptions constrained by a model of sulfide saturation. *Earth and Planetary Science Letters* **299**, 328–338.

Boudreau, A. (2016). Bubble migration in a compacting crystal-liquid mush. *Contributions to Mineralogy and Petrology* **171**, 32.

Bouvet de Maisonneuve, C., Dungan, M. A., Bachmann, O. & Burgisser, A. (2012a). Insights into shallow magma storage and crystallization at Volcán Llaima (Andean Southern Volcanic Zone, Chile). *Journal of Volcanology and Geothermal Research* **211–212**, 76–91.

Bouvet de Maisonneuve, C., Dungan, M. A., Bachmann, O. & Burgisser, A. (2012b). Petrological insights into shifts in eruptive styles at Volcán Llaima (Chile). *Journal of Petrology* **54**, 393–420.

Bottinga, Y. & Weill, D. (1972). The viscosity of magmatic silicate liquids: a model for calculation. *American Journal of Science* **272**, 438–475.

Brounce, M. N., Kelley, K. A. & Cottrell, E. (2014). The $Fe^{3+}/\sum Fe$ variations in Mariana Arc basalts and primary fO_2 of the mantle wedge. *Journal of Petrology* **55**, 2513–2536.

Bucholz, C. E., Gaetani, G. A., Behn, M. D. & Shimizu, N. (2013). Post-entrapment modification of volatiles and oxygen fugacity in olivine-hosted melt inclusions. *Earth and Planetary Science Letters* **374**, 145–155.

Burton, M. R., Mader, H. M. & Polacci, M. (2007). The role of gas percolation in quiescent degassing of persistently active basaltic volcanoes. *Earth and Planetary Science Letters* **264**, 46–60.

Cashman, K. V. (2004). Volatile controls on magma ascent and eruption. In: Sparks, R. S. J. & Hawkesworth, C. J. (eds) *The State of the Planet: Frontiers and Challenges in Geophysics. American Geophysical Union, Geophysical Monograph* **150**, doi:10.1029/150GM10.

Castro, J. M., Dingwell, D. B., Nichols, A. R. L. & Gardner, J. E. (2005). New insights on the origin of flow bands in obsidian. In: Manga, M. & Ventura, G. (eds) *Kinematics and Dynamics of Lava Flows. Geological Society of America, Special Papers* **396**, 55–66.

Cembrano, J. & Lara, L. (2008). The link between volcanism and tectonics in the southern volcanic zone of the Chilean Andes: A review. *Tectonophysics* **471**, 96–113.

Cervantes, P. & Wallace, P. (2003). Magma degassing and basaltic eruption styles: a case study of 2000 year BP Xitle volcano in central Mexico. *Journal of Volcanology and Geothermal Research* **120**, 249–270.

Cimarelli, C., Di Traglia, F. & Taddeucci, J. (2010). Basaltic scoria textures from a zoned conduit as precursors to violent Strombolian activity. *Geology* **38**, 439–442.

Cimarelli, C., Costa, A., Mueller, S. & Mader, H. M. (2011). Rheology of magmas with bimodal crystal size and shape distributions: Insight from analog experiments. *Geochemistry, Geophysics, Geosystems* **12**(**7**), doi:10.1029/2011GC003606.

Coltelli, M., Del Carlo, P., Pompillio, M. & Vezzoli, L. (2005). Explosive eruption of a picrate: The 3930 BP subplinian eruption of Etna volcano (Italy). *Geophysical Research Letters* **32**, L23307, doi:10.1029/2005GL024271.

Costa, A., Blake, S. & Self, S. (2006). Segregation processes in vesiculating crystallizing magmas. *Jou rnal of Volcanology and Geothermal Research* **153**, 287–300.

Cottrell, E., Kelley, K. A., Lanzirotti, A. & Fischer R. A. (2009). High-precision determination of iron oxidation state in silicate glasses using XANES. *Chemical Geology* **268**, 167–179.

Cottrell, E., Spiegelman, M. & Langmuir, C. H. (2002). Consequences of diffusive reequilibration for the interpretation of melt inclusions. *Geochemistry, Geophysics, Geosystems* **3**(**5**), doi:/10.1029/2001GC000205.

Couch, S., Sparks, R. S. J. & Carroll, M. R. (2003). The kinetics of degassing-induced crystallization at SoufriÒre Hills Volcano, Montserrat. *Journal of Petrology* **44**, 1477–1502.

Crabtree, S. M. & Lange, R. A. (2011). Complex phenocryst textures and zoning patterns in andesites and dacites: Evidence of degassing-induced rapid crystallization? *Journal of Petrology* **52**, 3–38.

Danyushevsky, L. V. & Plechov, P. (2011). Petrolog3: Integrated software for modeling crystallization processes. *Geochemistry, Geophysics, Geosystems* **12**(**7**), doi:10.1029/2011GC003516.

Danyushevsky, L. V., Della-Pasqua, F. N. & Sokolov, S. (2000). Re-equilibration of melt inclusions trapped by magnesian olivine phenocrysts from subduction-related magmas: petrological implications. *Contributions to Mineralogy and Petrology* **138**, 68–83.

Danyushevsky, L. V., McNeill, A. W. & Sobolev, A. V. (2002). Experimental and petrological studies of melt inclusions in phenocrysts from mantle-derived magmas: an overview of techniques, advantages and complications. *Chemical Geology* **183**, 5–24.

Deer, W. A., Howie, R. A. & Zussman, J. (1992). *An Introduction to the Rock-Forming Minerals*. Longman.

Del Bello, E., Lane, S. J., James, M. R., Llewellin, E. W., Taddeucci, J., Scarlato, P. & Capponi, A. (2015). Viscous plugging can enhance and modulate explosivity of strombolian eruptions. *Earth and Planetary Science Letters* **423**, 210–218.

Delgado, F., Pritchard, M.E., Ebmeier, S., González, P. & Lara, L. (submitted) Recent unrest (2002-2015) imaged by space geodesy at high risk Chilean volcanoes: Llaima, Villarrica and Calbuco (Southern Andes). Journal of Volcanology and Geothermal Research.

Dixon, J. E. & Stolper, E. M. (1995). An experimental study of water and carbon dioxide solubilities in mid-ocean ridge basaltic liquids. Part II: Applications to degassing. *Journal of Petrology* **36**, 1633–1646.

Dixon, J. E., Stolper, E. M. & Holloway, J. R. (1995). An experimental study of water and carbon dioxide solubilities in mid-ocean ridge basaltic liquids. Part I: Calibration and solubility models. *Journal of Petrology* **36**, 1607–1631.

Dungan, M. A., Long, P. E. & Rhodes, J. M. (1978). Magma mixing at mid-ocean ridges: evidence from legs 45 and 45-DSDP. *Geophysical Research Letters* **5**, 423–425.

Dzierma, Y. & Wehrmann, H. (2010). Eruption time series statistically examined: probabilities of future eruptions at Villarrica and Llaima Volcanoes, Southern Volcanic Zone, Chile. *Journal of Volcanology and Geothermal Research* **193**, 82–92.

Edmonds, M., Kohn, S. C., Hauri, E. H., Humphreys, M. C. S. & Cassidy, M. (2016). Extensive, water-rich magma reservoir beneath southern Montserrat. *Lithos* **252–253**, 216–233.

Erlund, E. J., Cashman, K. V., Wallace, P. J., Pioli, L., Rosi, M., Johnson, E. & Delgado Granados, H. (2010). Compositional evolution of magma from Parícutin Volcano, Mexico: The tephra record. *Journal of Volcanology and Geothermal Research* **197**, 167–187.

Ford, C. E., Russell, D. G., Groven, J. A. & Fisk, M. R. (1983). Distribution coefficients of Mg2+, Fe2+, Ca2+ and Mn2+ between olivine and melt. *Journal of Petrology* **24**, 256–265.

Fournier, T. J., Pritchard, M. E. & Riddick, S. N. (2010). Duration, magnitude, and frequency of subaerial volcano deformation events: New results from Latin America using InSAR and a global synthesis. *Geochemistry, Geophysics, Geosystems* Q01003, doi:10.1029/2009GC002558.

Francalanci, L., Tommasini, S. & Conticelli, S. (2004). The volcanic activity of Stromboli in the 1906–1998 AD period: mineralogical, geochemical and isotopic data relevant to the understanding of the plumbing system. *Journal of Volcanology and Geothermal Research* **131**, 179–211.

Francis, P. W., Glaze, L. S., Pieri, D., Oppenheimer, C. M. M., & Rothery, D. A. (1990). Eruption terms. *Nature* **346**, 519.

Gaetani, G. A., O'Leary, J. A., Shimizu, N., Bucholz, C. E. & Newville, M. (2012). Rapid reequilibration of H2O and oxygen fugacity in olivine-hosted melt inclusions. *Geology* **40**, 915–918.

Genereau, K., Valentine, G. A., Moore, G. & Hervig, R. L. (2010). Mechanisms for transition in eruptive style at a monogenetic scoria cone revealed by microtextural analyses (Lathrop Wells volcano, Nevada, U.S.A.). *Bulletin of Volcanology* **72**, 593–607.

Global Volcanism Program (2008). Report on Llaima (Chile). *Bulletin of the Global Volcanism Network* **33**(**6**), http://dx.doi.org/10.5479/si.GVP.BGVN200806-357110.

Govindaraju, K. (1994). Compilation of working values and sample description for 383 geostandards. *Geostandards Newsletter* **18**, 1–158.

Hammer, J. E. (2008). Experimental studies of the kinetics and energetics of magma crystallization. In: Putirka, K. D. & Tepley, F. J., III (eds) *Minerals, Inclusions and Volcanic Processes. Mineralogical Society of America and Geochemical Society, Reviews in Mineralogy and Geochemistry* **69**, 9–59.

Hantke, G. (1962). Übersicht über die vulkanische Tätigkeit 1957–1959. *Bulletin Volcanologique* **24**, 321–348.

Hayward, C. (2011). High spatial resolution probe microanalysis of tephras and melt inclusions without beam-induced chemical modification. *Holocene* **22**, 119–125.

Helo, C., Longprém, M.-A., Shimizu, N., Clague, D. A. & Stix, J. (2011). Explosive eruptions at mid-ocean ridges driven by CO2-rich magmas. *Nature Geoscience* **4**, 260–263.

Hervig, R. L., Mazdab, F. K., Moore, G. & McMillan, P. F. (2003). Analyzing hydrogen (H2O) in silicate glass by secondary ion mass spectrometry and reflectance Fourier transform infrared spectroscopy. *Developments in Volcanology* **5**, 83–103.

Hickey-Vargas, R. L., Frey, F. A. & Gerlach, D. C. (1986). Multiple sources for basaltic arc rocks from the Southern Volcanic Zone of the Andes (34°–41°S): Trace element and isotopic evidence for contributions from subducted oceanic crust, mantle, and continental crust. *Journal of Geophysical Research* **91**(**B6**), 5963–5983.

Higgins, M. D. (2000). Measurement of crystal size distributions. *American Mineralogist* **85**, 1105–1116.

Higgins, M. D. (2006). *Quantitative Textural Measurements in Igneous and Metamorphic Petrology*. Cambridge: Cambridge University Press.

Higgins, M. D. & Roberge, J. (2003). Crystal size distribution (CSD) of plagioclase and amphibole from Soufrière Hills volcano, Montserrat: evidence for dynamic crystallization/textural coarsening cycles. *Journal of Petrology* **44**, 1401–1411.

Houghton, B. F. & Gonnermann, H. M. (2008). Basaltic explosive volcanism: Constraints from deposits and models. *Chemie der Erde* **68**, 117–140.

Houghton, B. F. & Wilson, C. J. N. (1989). A vesicularity index for pyroclastic deposits. *Bulletin of Volcanology* **51**, 451–462.

Jacques, G., Hoernle, K., Gill, J., Wehrmann, H., Bindemann, I. & Lara, L. E. (2014). Geochemical variations in the Central Southern Volcanic Zone, Chile (38–43°S): The role of fluids in generating arc magmas. *Chemical Geology* **371**, 27–45.

Jaupart, C. (1998). Gas loss from magmas through conduit walls during eruption. In: Gilbert, J. S. & Sparks, R. S. J. (eds) *The Physics of Explosive Volcanic Eruptions*. Geological Society, London, Special Publications **145**, 73–90.

Jochum, K. P., Stoll, B., Herwig, K., et al. (2006). MPI-DING reference glasses for in situ microanalysis: New reference values for element concentrations and isotope ratios. *Geochemistry, Geophysics, Geosystems* **7**(**2**), doi:10.1029/2005GC001060.

Johnson, E. R., Wallace, P. J., Cashman, K. V., Delgado Granados, H. & Kent, A. J. R. (2008). Magmatic volatile contents and degassing-induced crystallization at Volcán Jorullo, Mexico: Implications for melt evolution and the plumbing systems of monogenetic volcanoes. *Earth and Planetary Science Letters* **269**, 478–487.

Johnson, E. R., Wallace, P. J., Cashman, K. V. & Delgado Granados, H. (2010). Degassing of volatiles (H2O, CO2, S, Cl) during ascent, crystallization, and eruptions at mafic monogenetic volcanoes in central Mexico. *Journal of Volcanology and Geothermal Research* **197**, 225–238.

Kazahaya, K., Shinohara, H. & Saito, G. (1994). Excessive degassing of Izu-Oshima volcano: magma convection in a conduit. *Bulletin of Volcanology* **56**, 207–216.

Kelley, K. A. & Cottrell, E. (2009). Water and the oxidation state of subduction zone magmas. *Science* **325**, 605–607.

Kelley, K. A. & Cottrell, E. (2012). The influence of magmatic differentiation on the oxidation state of Fe in a basaltic arc magma. *Earth and Planetary Science Letters* **329–330**, 109–121.

Kelley, K. A., Plank, T., Ludden, J. & Staudigel, H. (2003). Composition of altered oceanic crust at ODP Sites 801 and 1149. *Geochemistry, Geophysics, Geosystems* **4**(**6**), 8910, doi:10.1029/2002GC000435.

Kent, A. J. R. (2008). Melt inclusions in basaltic and related volcanic rocks. In: Putirka, K. D. & Tepley, F. J., III (eds) *Minerals, Inclusions and Volcanic Processes. Mineralogical Society of America and Geochemical Society, Reviews in Mineralogy and Geochemistry* **69**, 273–331.

Kress, V. C. & Carmichael, I. S. E. (1991). The compressibility of silicate liquids containing Fe2O3 and the effect of composition, temperature, oxygen fugacity and pressure on their redox states. *Contributions to Mineralogy and Petrology* **108**, 82–92.

Laiolo, M. & Cigolini, C. (2006). Mafic and ultramafic xenoliths in San Bartolo lava field: New insights on the ascent and storage of Stromboli magmas. *Bulletin of Volcanology* **68**, 653–670.

Landi, P., Métrich, N., Bertagnini, A. & Rosi, M. (2004). Dynamics of magma mixing and degassing recorded in plagioclase at Stromboli (Aeolian Archipelago, Italy). *Contributions to Mineralogy and Petrology* **147**, 213–227.

Lange, R. A., Frey, H. M. & Hector, J. (2009). A thermodynamic model for the plagioclase–liquid hygrometer/thermometer. *American Mineralogist* **94**, 494–506.

Lautze, N. C. & Houghton, B. F. (2007). Linking variable explosion style and magma textures during 2002 at Stromboli volcano, Italy. *Bulletin of Volcanology* **69**, 445–460.

Lloyd, A. S., Plank, T., Ruprecht, P., Hauri, E. H. & Rose, W. (2013). Volatile loss from melt inclusions in pyroclasts of differing sizes. *Contributions to Mineralogy and Petrology* **165**, 129–153.

Lofgren, G. (1974). An experimental study of plagioclase crystal morphology: Isothermal crystallization. *American Journal of Science* **274**, 243– 273.

Lucassen, F., Trumbull, R., Franz, G., Creixell, C., Vásquez, P., Romer, R. L. & Figueroa, O. (2004). Distinguishing crustal recycling and juvenile additions at active continental margins: the Paleozoic to recent composition evolution of the Chilean Pacific margin (36–41°S). *Journal of South American Earth Sciences* **17**, 103–119.

Luhr, J. F. (2001). Glass inclusions and melt volatile contents at Parícutin Volcano, Mexico. *Co ntributions to Mineralogy and Petrology* **142**, 261–283.

Lytle, M. L., Kelley, K. A., Hauri, E. H., Gill, J. B., Papia, D. & Arculus, R. J. (2012). Tracing mantle sources and Samoan influence in the northwestern Lau back-arc basin. *Geochemistry, Geophysics, Geosystems* **13**(**10**), Q10019, doi:10.1029/2012GC004233.

Mandeville, C. W., Sasaki, A., Saito, G., Faure, K., King, R. & Hauri, E. (1998). Open-system degassing of sulfur from Krakatau 1883 magma. *Earth and Planetary Science Letters* **160**, 709–722.

Mangan, M. T. & Cashman, K. V. (1996). The structure of basaltic scoria and reticulate and inferences for vesiculation, foam formation, and fragmentation in lava fountains. *Journal of Volcanology and Geothermal Research* **73**, 1–18.

Marsh, B. D. (1998). On the interpretation of crystal size distributions in magmatic systems. *Journal of Petrology* **39**, 553–599.

Menand, T. & Phillips, J. C. (2007). Gas segregation in dykes and sills. *Journal of Volcanology and Geothermal Research* **159**, 393–408.

Métrich, N. & Wallace, P. J. (2008). Volatile abundances in basaltic magmas and their degassing paths tracked by melt inclusions. In: Putirka, K. D. & Tepley, F. J., III (eds) *Minerals, Inclusions and Volcanic Processes. Mineralogical Society of America and Geochemical Society, Reviews in Mineralogy and Geochemistry* **69**, 363–402.

Métrich, N., Bertagnini, A., Landi, P. & Rosi, M. (2001). Crystallization driven by decompression and water loss at Stromboli Volcano (Aeolian Island, Italy). *Journal of Petrology* **42**, 1471–1490.

Métrich, N., Bertagnini, A. & Di Muro, A. (2010). Conditions of magma storage, degassing and ascent at Stromboli: new insights into the volcano plumbing system with inferences on the eruptive dynamics. *Journal of Petrology* **51**, 603–626.

Moitra, P., Gonnermann, H. M., Houghton, B. F. & Giachetti, T. (2013). Relating vesicle shape in pyroclasts to eruption styles. *Bulletin of Volcanology* **75**, 691, doi:10.1007/s00445-013-0691-8.

Moore, G. (2008). Interpreting H2O and CO2 contents in melt inclusions: Constraints from solubility experiments and modeling. In: Putirka, K. D. & Tepley, F. J., III (eds) *Minerals, Inclusions and Volcanic Processes. Mineralogical Society of America and Geochemical Society, Reviews in Mineralogy and Geochemistry* **69**, 333–361.

Moreno, H. & Fuentealba, G. (1994). The May 17–19 1994 Llaima Volcano eruption, Southern Andes (38°42′S, 71°44′W). *Revista Geológica de Chile* **21**, 167–171.

Morgan, D. J. & Jerram, D. A. (2006). On estimating crystal shape for crystal size distribution analysis. *Journal of Volcanology and Geothermal Research* **154**, 1–7.

Naranjo, J. A. & Moreno, H. (2005). *Geologíca del Volcan Llaima, Regíon de la Araucanía. Carta Geológica de Chile, Serie Geológica Básica*. Santiago: Servicio Nacional de Geología y Minería, 88 pp.

Neave, D. A., Maclennan, J., Edmonds, M. & Thordarson, T. (2014). Melt mixing causes negative correlation of trace element enrichment and CO2 content prior to an Icelandic eruption. *Earth and Planetary Science Letters* **400**, 272–283.

Newman, S. & Lowenstern, J. B. (2002). VolatileCalc: A silicate melt–H2O–CO2 solution model written in Visual Basic for Excel. *Computers and Geosciences* **28**, 597–604.

Newman, S., Stolper, E. & Stern, R. (2000). H2O and CO2 in magmas from the Mariana arc and back arc systems. *Geochemistry, Geophysics, Geosystems* **1**(**1**), doi:10.1029/1999GC000027.

Nichols, A. R. L. & Wysoczanski, R. J. (2007). Using micro-FTIR spectroscopy to measure volatile contents in small and unexposed inclusions hosted in olivine crystals. *Chemical Geology* **242**, 371–384.

ONEMI. (2009). Actividad VolcÃnica en Chile, Aþo 2008. Gobierno de Chile Ministerio del Interior, Santiago, Chile, 60 pp.

Oppenheimer, C., Moretti, R., Kyle, P. R., Eschenbacher, A., Lowenstern, J. B., Hervig, R. L. & Dunbar, N. W. (2011). Mantle to surface degassing of alkali magmas at Erebus volcano, Antarctica. *Earth and Planetary Science Letters* **306**, 261–271.

Palma, J. L., Blake, S. & Calder, E. S. (2011). Constraints on the rates of degassing and convection in basaltic open-vent volcanoes. *Geochemistry, Geophysics, Geosystems* **12**(**11**), Q11006, doi:10.1029/2011GC003715.

Pansino, S. (2012). Experimental analysis of bubble-driven mixing in a volcanic conduit and how it affects lava lake sustainability. MS thesis, University at Buffalo, NY, 59 pp.

Papale, P., Moretti, R. & Barbato, D. (2006). The compositional dependence of the saturation surface of H2O + CO2 fluids in silicate melts. *Chemical Geology* **229**, 78–95.

Parfitt, E. A. & Wilson, L. (1995). Explosive volcanic eruptions—IX. The transition between Hawaiian-style lava fountaining and Strombolian explosive activity. *Geophysical Journal International* **121**, 226–232.

Petit-Breuilh, M. E. (2006). *La Historia Eruptiva de los Volcanes Hispanoamericanos (Siglos XVI al XX)*. Huelva: Servicio de Publicaciones del Cabildo Insular de Lanzarote.

Pioli, L., Erlund, E., Johnson, E., Cashman, K., Wallace, P., Rosi, M. & Delgado Granados, H. (2008). Explosive dynamics of violent Strombolian eruptions: The eruption of Parícutin Volcano 1943–1952 (Mexico). *Earth and Planetary Science Letters* **271**, 359–368.

Pioli, L., Azzopardi, B. J. & Cashman, K. V. (2009). Controls on the explosivity of scoria cone eruptions: Magma segregation at conduit junctions. *Journal of Volcanology and Geothermal Research* **186**, 407–415.

Pistone, M., Arzilli, F., Dobson, K. J., Cordonnier, B., Reusser, E., Ulmer, P., Marone, F., Whittington, A. G., Mancini, L., Fife, J. L. & Blundy, J. D. (2015). Gas-driven filter pressing in magmas: Insights into in-situ melt segregation from crystal mushes. *Geology* **43**, 699.

Polacci, M., Corsaro, R. A. & Andronico, D. (2006). Coupled textural and compositional characterization of basaltic scoria: Insights into the transition from Strombolian to fire fountain activity at Mount Etna, Italy. *Geology* **34**, 201–204.

Portnyagin, M., Almeev, R., Matveev, S. & Holtz, F. (2008). Experimental evidence for rapid water exchange between melt inclusions in olivine and host magma. *Earth and Planetary Science Letters* **272**, 541–552.

Preece, K., Gertisser, R., Barclay, J., Charbonnier, S. J., Komorowski, J.-C. & Herd, R. A. (2016). Transitions between explosive and effusive phases during the cataclysmic 2010 eruption of Merapi volcano, Java, Indonesia. *Bulletin of Volcanology* **78**, 54.

Putirka, K. D. (2008). Thermometers and barometers for volcanic systems. In: Putirka, K. D. & Tepley, F. J., III (eds) *Minerals, Inclusions and Volcanic Processes. Mineralogical Society of America and Geochemical Society, Reviews in Mineralogy and Geochemistry* **69**, 61–120.

Putirka, K. D., Perfit, M., Ryerson, F. J. & Jackson, M. G. (2007). Ambient and excess mantle temperatures, olivine thermometry, and active vs. passive upwelling. *Chemical Geology* **241**, 177–206.

Reichen, L. E. & Fahey, J. J. (1962). An improved method for the determination of FeO in rocks and minerals including garnet. *US Geological Survey Bulletin* **1144(B)**, 1–5.

Remy, D., Chen, Y., Froger, J. L., Bonvalot, S., Cordoba, L. & Fustos, J. (2015). Revised interpretation of recent InSAR signals observed at Llaima volcano (Chile). *Geophysical Research Letters* doi:10.1002/2015GL063872.

Reubi, O., Bourdon, B., Dungan, M. A., Koorneef, J. M., Sellés, D., Langmuir, C. H. & Aciego, S. (2011). Assimilation of the plutonic roots of the Andean arc controls variations in U-series disequilibria at Volcan Llaima, Chile. *Earth and Planetary Science Letters* **303**, 37–47.

Rhodes, J. M., Dungan, M. A., Blanchard, D. P. & Long, P. E. (1979). Magma mixing at mid-ocean ridges: evidence from basalts drilled near 22°N on the mid-Atlantic ridge. *Tectonophysics* **55**, 35–61.

Roeder, P. L. & Emslie, R. F. (1970). Olivine–liquid equilibrium. *Contributions to Mineralogy and Petrology* **29**, 275–289.

Roggensack, K., Hervig, R. L., McKnight, S. B. & Williams, S. N. (1997). Explosive basaltic volcanism from Cerro Negro volcano: Influences of volatiles on eruptive style. *Science* **277**, 1639–1642.

Rose, W. I., Palma, J. L., Delgado Granados, H. & Varley, N. (2013). Open-vent volcanism and related hazards: Overview. In: Rose, W. I., Palma, J. L., Delgado Granados, H. & Varley, N. (eds) *Understanding Open-vent Volcanism and Related Hazards*. Geological Society of America, Special Papers 498, vii–xiii, doi:10.1130/2013.2498(00).

Rose, W. I., Self, S., Murrow, P. J., Bonadonna, C., Durant, A. J. & Ernst, G. G. J. (2008). Nature and significance of small volume fall deposits at composite volcanoes: Insights from the October 14, 1974 Fuego eruption, Guatemala. *Bulletin of Volcanology* **70**, 1043–1067.

Rosi, M., Bertagnini, A. & Landi, P. (2000). Onset of the persistent activity at Stromboli Volcano (Italy). *Bulletin of Volcanology* **62**, 294–300.

Rosi, M., Pistolesi, M., Bertagnini, A., Landi, P., Pompilio, M. & Di Roberto, A. (2013). Stromboli volcano, Aeolian Islands (Italy): present eruptive activity and hazards, In: Lucchi, F., Peccerillo, A., Keller, T. & Tranne, C. A. (eds) *The Aeolian Island Volcanoes*. Geological Society, London, Memoirs **37**, 473–490.

Ruth, D. C. S. (2014). Physical and geochemical systematics of the 2008 violent Strombolian eruption of Llaima volcano, Chile. PhD dissertation, University at Buffalo, NY, 203 pp.

Ruth, D. C. S. & Calder, E. S. (2014). Plate tephra: Preserved bubble walls from large slug bursts during violent Strombolian eruptions. *Geology* **42**, 11–14.

Sable, J. E., Houghton, B. F., Del Carlo, P. & Coltelli, M. (2006). Changing conditions of magma ascent and fragmentation during the Etna 122 BC basaltic Plinian eruption: Evidence from clast microtextures. *Journal of Volcanology and Geothermal Research* **158**, 333–354.

Schonwalder-Angel, D. A. (2015). The emplacement of satellite scoria cones at Llaima Volcanic System, Chile: The interaction between magmatic overpressure and the local tectonics. PhD dissertation, University at Buffalo, NY, 280 pp.

Shaw, H. R. (1972). Viscosities of magmatic silicate liquids: An empirical method of prediction. *American Journal of Science* **272**, 870–893.

Sisson, T. W. & Bacon, C. R. (1999). Gas-driven filter pressing in magmas. *Geology* **27**, 613–616.

Stevenson, D. S. & Blake, S. (1998). Modelling the dynamics and thermodynamics of volcanic degassing. *Bulletin of Volcanology* **60**, 307–317.

Stolper, E. M. (1982a). Water in silicate glasses: An infrared spectroscopic study. *Contributions to Mineralogy and Petrology* **81**, 1–13.

Stolper, E. M. (1982b). The speciation of water in silicate melts. *Geochimica and Cosmochimica Acta* **46**, 2609–2620.

Streck, M. J. (2008). Mineral textures and zoning as evidence for open system processes. In: Putirka, K. D. & Tepley, F. J., III (eds) *Minerals, Inclusions and Volcanic Processes. Mineralogical Society of America and Geochemical Society, Reviews in Mineralogy and Geochemistry* **69**, 623–649.

Streck, M. J., Dungan, M. A., Malavassi, E., Reagan, M. K. & Bussy, F. (2002). The role of basalt replenishment in the generation of basaltic andesites of the ongoing activity at Arenal volcano, Costa Rica: evidence from clinopyroxene and spinel. *Bulletin of Volcanology* **64**, 316–327.

Sun, S.-S. & McDonough, W. F. (1989). Chemical and isotopic systematics of ocean basalts: implications for mantle compositions and processes. In: Saunders, A. D. & Norry, M. J. (eds) *Magmatism in the Ocean Basins*. Geological Society, London, Special Publications **42**, 313–345.

Thomas, N., Tait, S. & Koyaguchi, T. (1993). Mixing of stratified liquids by the motion of gas bubbles: application to magma mixing. *Earth and Planetary Science Letters* **115**, 161–175.

Toplis, M. J. & Carroll, M. R. (1995). An experimental study of the influence of oxygen fugacity on Fe–Ti oxide stability, phase relations, and mineral–melt equilibria in ferro-basaltic systems. *Journal of Petrology* **36**, 1137–1170.

Tran, A., Rudolph, M. L. & Manga, M. (2015). Bubble mobility in mud and magmatic volcanoes. *Journal of Volcanology and Geothermal Research* **294**, 11–24.

Valentine, G. A. & Gregg, T. K. P. (2008). Continental basaltic volcanoes—processes and problems. *Journal of Volcanology and Geothermal Research* **177**, 857–873.

Vergniolle, S. & Jaupart, C. (1990). Dynamics of degassing at Kilauea Volcano, Hawaii. *Journal of Geophysical Research* **95**(**B3**), 2793–2809.

Vinet, N. & Higgins, M. D. (2010). Magma solidification processes beneath Kilauea volcano, Hawaii: A quantitative textural and geochemical study of the 1969–1974 Mauna Ulu lavas. *Journal of Petrology* **51**, 1297–1332.

Voight, B., Widiwijayanti, C., Mattioli, G., Elsworth, D., Hidayat, D. & Strutt, M. (2010). Magma-sponge hypothesis and stratovolcanoes: Case for a compressible reservoir and quasi-steady deep influx at Soufrière Hills Volcano, Montserrat. *Geophysical Research Letters* **37**, L00E05, doi:10.1029/2009GL041732.

Wallace, P. J., Kamenetsky, V. S. & Cervantes, P. (2015). Melt inclusion CO2 contents, pressures of olivine crystallization, and the problem of shrinkage bubbles. *American Mineralogist* **100**, 787–794.

Williams, S. N. (1983). Plinian airfall deposits of basaltic composition. *Geology* **11**, 211–214.